

## Lessons Learnt from the Ultra-Micro Gas Turbine Development at University of Tokyo

**Toshio NAGASHIMA et al.**

Department of Aeronautics and Astronautics  
University of Tokyo  
7-3-1, Hongo, Bunkyo  
Tokyo 113-8656  
JAPAN

[tnaga@mail.ecc.u-tokyo.ac.jp](mailto:tnaga@mail.ecc.u-tokyo.ac.jp)

### **ABSTRACT**

*The outcome of NEDO supported international research project led by University of Tokyo is reviewed, with respect to developing key technologies for ultra-micro gas turbines (UMGT). The study suggested 'Finger-top' gas turbines as a currently feasible extreme that install rotors of 8 mm in diameter with 1.2 million rpm to produce tens of watts net output. Prior to practicing such UMGT system integration, 'Palm-top' gas turbine engine of an expected 2 – 3 kW output was first prototyped to operate successfully under a measurable control system, using propane as the fuel and installing a compact heat exchanger, which yielded valuable conceptual as well as practical data base for further advancement of UMGT designing.*

### **1. PROJECT OVERVIEW AND RESEARCH CONSORTIUM [1, 2, 3-11]**

The project started in FY2001 and ended in FY2003 with an aim of establishing key technologies for use in a small reusable mobile power source with high power and energy density that is driven by an ultra micro gas turbine system. The outcome is expected to contribute to realize not only a compact energy conversion system, but also spin-off products relating to various components of that system.

In the first year (FY2001), a careful feasibility study was conducted about the potential application and technology innovation in developing such a smallest size of gas turbine system, in context of a proposal of Power-MEMS turbine by MIT. Though revolutionary in the sense of utilizing MEMS fabrication, a central issue was the simplest question whether it can work or not as an engine. It was (and yet is) very difficult to give a clear answer to it, since there exists no data available for producing such mm size turbo-engines.

As the first step, therefore, several key hardware components employed in MIT gas turbine system were designed and fabricated on a 10-times enlarged scale, so that detailed measurements, to some extent, might be accessible via the actual testing, which are otherwise quite impossible to carry out by employing currently available instrumentation. Consequent deficiency was obvious, since the most innovative part of the concept, MEMS fabrication, had to be lost, in addition to differences in thermo-fluid dynamic similarity parameters, rotor dynamics and structural materials, all in all, crucial for the estimation of gas turbine performance. It was however argued that the miniaturization to this order of 10 times enlargement, thus 100 times in the power output scale, is still worth challenge for progress and marketing of reusable mobile or distributable energy sources. A part of the lack in knowledge might be compensated by the help of computer simulation technology, for instance, CFD is getting profoundly useful tools for analyzing and designing the airflows in turbo-machinery. Three European collaborators, VKI, ONERA and CIAM

Nagashima, T. et al (2005) Lessons Learnt from the Ultra-Micro Gas Turbine Development at University of Tokyo. In *Micro Gas Turbines* (pp. 14-1 – 14-58). Educational Notes RTO-EN-AVT-131, Paper 14. Neuilly-sur-Seine, France: RTO. Available from: <http://www.rto.nato.int/abstracts.asp>.

contributed significantly to the last point, by employing their state-of-the-art software for the design and performance prediction of the 10 times enlarged turbo-components.

In the second year (FY2002), a step forward was taken to clarify the following project targets: (1) prototype Palm-top gas turbine engine, and (2) develop key components of Finger-top gas turbine system.

Palm-top is an idea based upon treating the above 10 times enlarged model into refined shape of practical usefulness, expecting for marketing products. MEMS fabrication is no longer of essential necessity, but conventional machining from forged or casting metals becomes more appropriate, so that manufacturing practice, in absence of active cooling, suggested to keep the maximum turbine inlet temperature, *TIT*, below 1223K (950C) from mechanical strength reason. While radial, rather than axial, rotor technology was judged indispensable for the engine compactness as well as in context of the leading configuration of Power-MEMS turbines, impeller blades were allowed for designing into 3D (dimensional) shape for the better aerodynamic performance. The lower *TIT*, thus less pressure ratio, in gas turbine cycle meant disadvantage for thermal efficiency, so that a crucial measure was taken to install a heat exchanger to make Palm-top feasible at the lower pressure ratio, by adopting regenerative cycle. Compactness is mandatory for Palm-top, so that a penalty of recuperator installation needed to be well compensated by the benefit in thermal efficiency, realizing the smallest possible fuel tank.

Finger-top, on the other hand, is by no means accounted for a marketing product in view of practical technology level, so that thorough research is needed for better performance of individual key components while minimizing the system compactness. A careful study on thermal balance between hot and cold components of Power-MEMS turbine revealed that significant cycle output loss, because of increased heat transfer associated with the engine size reduction, results in very little power derived from the original MIT turbine. Double the rotor size, however, yielded a comfortable increase of output power, thus the target rotor size of Finger-top was presently decided to 8 mm in diameter, which seemed also about the limit size of a disk on which 3D blade profiles were machined. Correspondingly, a micro channel recuperator was also designed to demonstrate optimization process of its channel width and length.

In the third year (FY2003), continued efforts were made for prototyping and testing Palm-top, as well as developing key components for use in Finger-top, aiming for essential improvements in performance and stability in operation.

Palm-top was fully equipped with turbo-components employing air bearings, annular combustor and recuperator which circumferentially surrounded the engine core. Test runs were successfully operated up to rotational speed of 160,000rpm at exhaust gas temperature of 1,000°C. In order to aim for further drastic improvement in efficiency and specific power, a wave rotor was besides designed and fabricated, which is yet to be integrated into the system, therefore, will be described elsewhere.

As for key components of Finger-top, design and fabrication process for the rotors with 8 mm in diameter were examined with respect to machining and tolerance, so that actually fabricated piece was inspected against geometry specification for a rotor with complex 3D blade profiles. The result was satisfactory for a promise of further development. Whilst the efforts so far were directed to 3D rotor design, similarly in Palm-top, for the better aerodynamic efficiency, 2D rotor design still needs explored in context of MEMS fabrication as well as simplicity in structural dimensions. CFD simulations were thus made for several 2D or 2.5D turbine and compressor rotors to clarify the effects of Reynolds number, tip clearance and heat transfer between adjacent components, upon total pressure loss within the turbo-passage flows. Pre-mixed micro flat-flame combustor with hydrogen fuel was also designed and tested for measurements of combustion characteristics. Preliminary tests on bonding process for silicon wafers were conducted to confirm manufacturing micro channels of 400µm square cross section for ultra-compact recuperator. Lastly, a motor/generator fit for separate installation was compared between electrostatic and magnetic types, so that an extremely small magnetic type was designed, fabricated and tested.

**Table 1: Total Plan of the Research Project**

FY2001	FY2002	FY2003
<ul style="list-style-type: none"> <li>⊙ <u>Target : realization of elements</u></li> <li>⊙ 10 times model (40mm)               <ul style="list-style-type: none"> <li>○ 2D turbines and compressors</li> <li>○ 3D turbines and compressors</li> <li>○ Can combustors</li> <li>○ Oil lubricated bearings</li> <li>○ Foil gas bearings</li> </ul> </li> <li>⊙ One and two times models               <ul style="list-style-type: none"> <li>○ Combustor (4mm) model tests</li> <li>○ Fabrication of blades(8mm)</li> </ul> </li> <li>⊙ Design and fabrication of test facilities and measurement system</li> </ul>	<ul style="list-style-type: none"> <li>⊙ <u>Target: design/fabrication of model GT</u></li> <li>⊙ Palm-top GT               <ul style="list-style-type: none"> <li>○ Design, fabrication, test</li> <li>○ Turbine blade diameter 40mm</li> <li>○ Compressor wheel diameter 44mm</li> <li>○ Annular combustor</li> <li>○ Recuperator</li> <li>○ Permanent magnet generator</li> </ul> </li> <li>⊙ Finger top GT               <ul style="list-style-type: none"> <li>○ Aerodynamic test blade (8mm)</li> <li>○ Design of test facilities</li> <li>○ Fabrication of recuperator</li> </ul> </li> </ul>	<ul style="list-style-type: none"> <li>⊙ <u>Target: realization of GT</u></li> <li>⊙ Palm-top GT               <ul style="list-style-type: none"> <li>○ Realization test</li> <li>○ Turbine inlet temp. 900°C</li> <li>○ Compressor PR. 2.5</li> <li>○ Generator output power 2kW</li> <li>○ Recuperator</li> <li>○ Control systems</li> </ul> </li> <li>⊙ Finger Top GT               <ul style="list-style-type: none"> <li>○ Aerodynamic test rig</li> <li>○ Engine design</li> <li>○ Out put power tens of W</li> </ul> </li> </ul>

**Table 2: Research Consortium**

Univ. Tokyo	Inst. Industrial Sciences	YOSHIKI, Haruo KATO, Chisachi MATSUO, Eito	Project leader Project co-leader, Turbine group head Fabrication group head
	Dept. Aero & Astronautics	NAGASHIMA, Toshio TERAMOTO, Susumu YAMAGUCHI, Kazuo OKAMOTO, Koji	Research leader CFD group head Fabrication Wave rotor group head
	Dept. Mechanical Eng.	KANEKO, Shigehiko	Bearing&Rotordynamics group head
Tokyo Metro. Inst. Tech.	Dept. Aerospace Eng.	YUASA, Saburo	Combustor group head
Gunma Univ.	Dept. Mechanical Eng.	OBOOKATA, Tomio ISHIMA, Tsuneaki	Meas. & Monitoring group head Measurement & Monitoring
Tokyo Inst. Tech.		NAGASAKI, Takao ITO, Yutaka	Heat Exchanger group head Heat Exchanger
Kyushu Univ.	Dept. Aerospace Eng.	YAMASAKI, Nobuhiko TAKAHASHI, Koji	CFD MEMS Fabrication
Kanagawa Inst. Tech.	Dept. System Design Eng.	ISHIHAMA, Masao KASHIWABARA, Yasunari	Electric Motor Generator Eelectric Motor Generator
Hosei Univ.	Dept. Mechanical Eng.	MIZUKI, Shinpei TSUJITA, Seiho MINORIKAWA, Manabu	Compressor group head Compressor Compressor
Waseda Univ.	Dept. Mechanical Eng.	YOSHIOKA, Eisuke OHTA, Akira	Compressor CFD
Keio Univ.	Dept. Mechanical Eng.	KAWAGUCHI, Osamu	Combustor
Tsukuba Inst. Tech.	Dept. Mechanical Eng.	NAKAZAWA, Norio	Fabrication
<b>Governmental</b>	JAXA	YOSHIDA, Toyoaki YAMANE, Takashi	Heat Exchanger CFD
	NEDO WE-NET Centre	OGATA, Hiroshi	Fabrication
	AI ST	TSUTSUI, Yasutaka	Micro-Mech. System
	JDA	YASUE, Masahiro	Adviser
<b>Industry</b>	Mitsubishi	AOKI, Teruyuki UCHIDA, Seishi	Fabrication Fabrication
	Ishikawajima-Harima	WATANABE, Yasuyuki	Fabrication
	Kawasaki	MORI, Kenji	Combustor
	Toshiba	NAGAO, Shinichiro UCHIDA, Tatsuro	Electric Motor Generator MEMS Fabrication, Motor Generator
	Hitachi	HAMATAKE, Hisashi	Fabrication
	Sumitomo Precision	TOKUE, Rinzo KASANO, Koichiro ICHIKAWA, Masamichi KASHIMA, Shoichi	Heat Exchanger MEMS Fabrication Heat Exchanger Heat Exchanger
<b>Overseas</b>	VKI	VAN DEN BRAEMBUSSCHE,R.	Research Collaborator
	ONERA	RIBAUD, Yves	Research Collaborator
	CIAM	IVANOV, M. Ja.	Research Collaborator

## 2. USEFULNESS AND SPIN-OFF [12-17]

There are numerous applications for mobile power sources, (Figure 1) which require energy density not attainable by batteries. Robots, small UAV (Unmanned Air Vehicles), exoskeletons and electric information terminals require power density in the range of 0.1~0.6 [kW/kg] as well as energy density of 0.2~6 [kWhr/kg]. For instance, currently the power density level needed for Aibo, Asimo and Ginger as shown in Figure 1 are 6~9 [W/kg] (output/total weight), so that engines of the corresponding power and energy density are actually at the stage of demand and practice. Superb power and energy density of gas turbines is attributable to distinguished specific chemical energy that fuels contain. A wide range of fuels can be used, for instance, most representatives being liquid hydrocarbon and gaseous fuels such as propane or hydrogen. UMGH is certainly envisioned as one of the best choices amongst various, including both ordinary and emergency, power supply that can enrich and help industrial activities and social welfare by providing various applications and opportunities for either mobile or highly distributed use, ultra micro propulsion systems for vehicles more than UAV, e.g. space and deep-water ones, auxiliary power units, hybrid with other power sources, in particular, fuel cells, as well as ultra micro turbo-machinery to list some like cooling apparatus, pumps, compressors that are all expectable spin-offs from UMGH component technology.

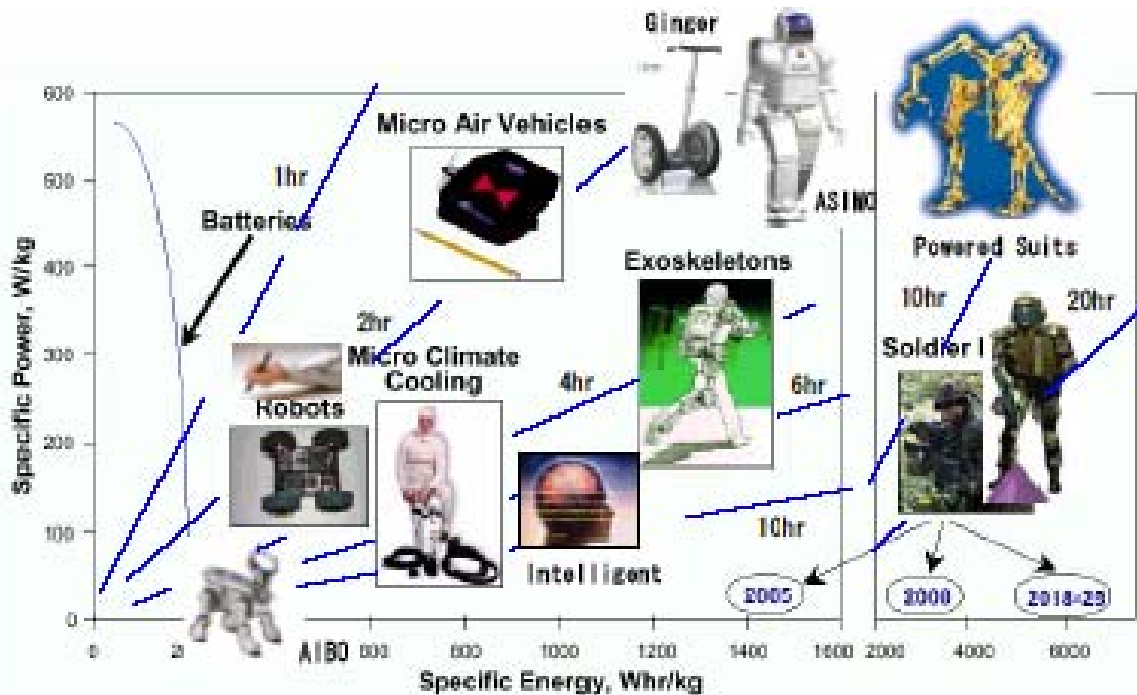


Figure 1: Specific Energy and Applications.

## 3. PLANNING

### 3.1 Cycle Design Point [1, 2, 17]

Compactness is mandatory for Palm-top, which has to take into account all the engine components including fuels. In cases when operation is for a long duration, fuel tank volume may become larger than the engine core. Since specific fuel consumption,  $SFC$ , is inversely proportional to thermal efficiency,  $\eta_{th}$ , it is essential to improve the latter for achieving reduction in engine size and weight. (The fuel choice may be also very influential.). Figure 2 illustrates the relationship between the required fuel tank volume  $V$  versus

thermal efficiency in reference to that at 10% thermal efficiency. At the lower efficiency, which is likely for the smaller engine core, more significant penalty will be imposed to the engine compactness.

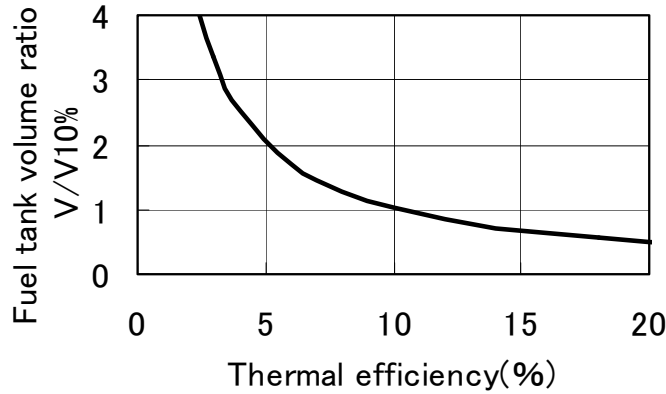


Figure 2: Thermal Efficiency vs. Fuel Tank Volume.

For better thermal efficiency, it is a straightforward thought to raise pressure and temperature ratio from the thermodynamic cycle point of view, needless to mention about attaining less component losses. Figure 3 presents the calculation results for a simple gas turbine cycle, whereby design point will be selected to determine specifications for Palm-top and Finger-top gas turbines. Here, MEMS fabrication is no longer of essential necessity, but conventional manufacturing becomes appropriate to eventually fix the maximum turbine inlet temperature  $TIT$  at 1223K (950C). Component efficiency  $\eta_{all}$  may be conveniently defined as the product of turbine, compressor, and mechanical efficiencies:  $\eta_{all} = \eta_T \eta_C \eta_m$ . Given the target component efficiency  $\eta_{all}$  of 57% for Palm-top and 45% for Finger-top, the peak thermal efficiency turns out to be approximately 15% and 7%, respectively, at each corresponding pressure ratio 7 or 4.

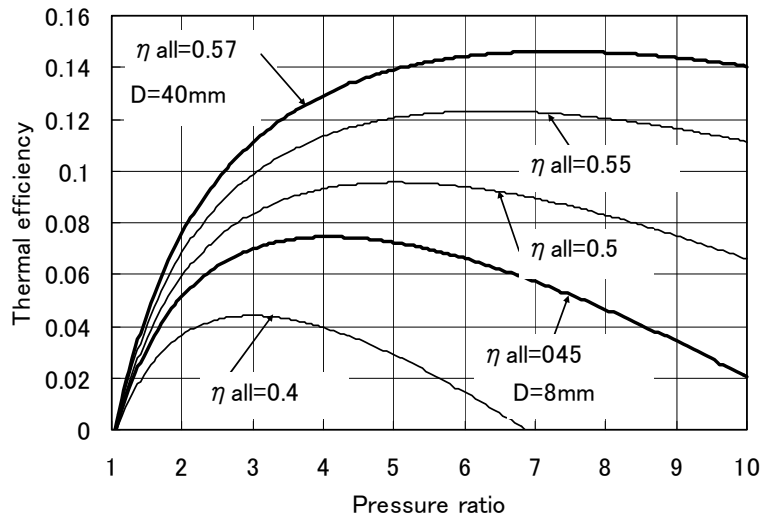
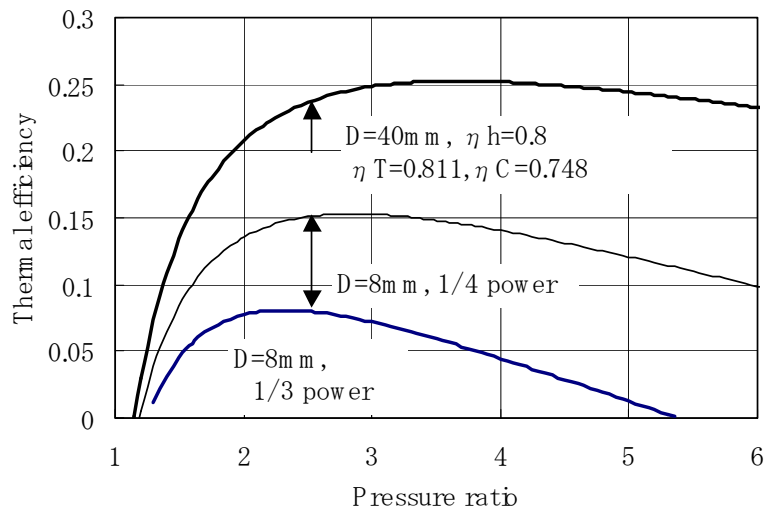


Figure 3: Thermal Efficiency of Simple Cycle UMG.

Profound improvement in thermal efficiency is attainable by increased component efficiency  $\eta_{all}$ , but it is also apparent that the optimum cycle pressure ratio needs to be raised to a great extent. For MIT original Power-MEMS turbine, the design pressure ratio was 4, which necessitated rotors of 4 mm in diameter at ultra-high revolution at 2.4 million rpm. That has to be definitely avoided for the present Palm-top system.

An alternative way is to shift into regenerative cycle. Every text on gas turbines states about the latter cycle benefits of substantial gain in thermal efficiency due to waste heat recovery and also lowering the optimum cycle pressure ratio, which seem to suit quite well to solve the present technical difficulties. So the question is concerned with system integrity, in other words, how come to match the size of heat exchanger or recuperator compatible with the engine core, without losing thermal and fluid-dynamic efficiencies in heat exchanging process. A penalty of attaching additional components may be compensated by reduction of fuel tank volume and weight, as mentioned earlier, if ultra-compact recuperator is realized with good performance at less volume, wherein it looks more promising to apply MEMS fabrication technology. Figure 4 shows plotting of calculation results of thermal efficiency versus pressure ratio for a regenerative cycle, where component efficiency is based upon Palm-top size ( $D=40\text{mm}$ , turbine and compressor efficiency of  $\eta_T=0.811$  and  $\eta_C=0.748$ , while recuperator thermal efficiency  $\eta_h=0.8$ ). The curves for Finger-top were derived by using  $Re$  number correction. Upon comparison with Figure 3, thermal efficiency is improved almost double, thus saving half of the fuel tank volume, whilst the engine volume was predicted to become 3 times larger by attaching a recuperator. It is a balance that matters between reduction and attachment in volume, associated with either fuel tank or recuperator, while significant ease in rotational speed needs again to be stressed to find the optimum pressure ratio getting down to 2.5. The gain in thermal efficiency is also much affected by the index in  $Re$  number correction, thus it is the first priority to keep component efficiency  $\eta_{all}$  good enough to accommodate the benefit. Based upon the foregoing considerations, together with mechanical integrity, the design specification was set as listed in Table 3.



**Figure 4: Thermal Efficiency of Regenerated UMG.**

**Table 3: Design Feature**

	Palm-top	Finger-top
Compressor PR	2.5	2.5
TIT (K)	1223	1223
Flow rate (kg/s)	0.03	0.0011
Rotational speed (rpm)	235,000	1,170,000
Turbine diameter (mm)	40	8



### 3.2 Finger-Top and Palm-Top Sizing

Palm-top aims for 2~3 kW output, while Finger-top is expected to produce tens of watts, with power density superior to Power-MEMS turbines by means of system integration with ultra-compact recuperator for regenerative cycle. It will be, from engineering point of view, the best solution to explore such miniature turbines of mm size with certain feasibility, since the maximum cycle temperature and pressure ratio are at least within-reach of the past manufacturing experience. Palm-top could be the world's smallest and lightest with dry weight of 14.3kg including the generator, while cubic volume of 8.5 liters. Nevertheless, there is obviously enormous lack in knowledge and practice to design key components relating to Palm- and Finger-top gas turbine systems, which will be explained in the next. A point to be addressed, here, is that heat conduction between hot and cold components plays a crucial role in deteriorating the engine performance. In order to produce thermodynamic work, heat loss via wall conduction should be kept as small as possible, which becomes very difficult as the engine gets thus far miniaturized. A detailed study [18] resulted in very little power out from MIT original Power-MEMS turbines with rotors of 4 mm in diameter, while double the rotor diameter showed marginal increase in power. Other considerations towards machining tolerance, shaft diameter for air bearings and rotor dynamics, motor-generator coupling, and most importantly, recuperator integration, all in all, indicated the minimum rotor size to be 8 mm in diameter for manufacturing, thus, chosen as the rotor tip diameter for Finger-top, presently.

## 4. PALM-TOP TESTING

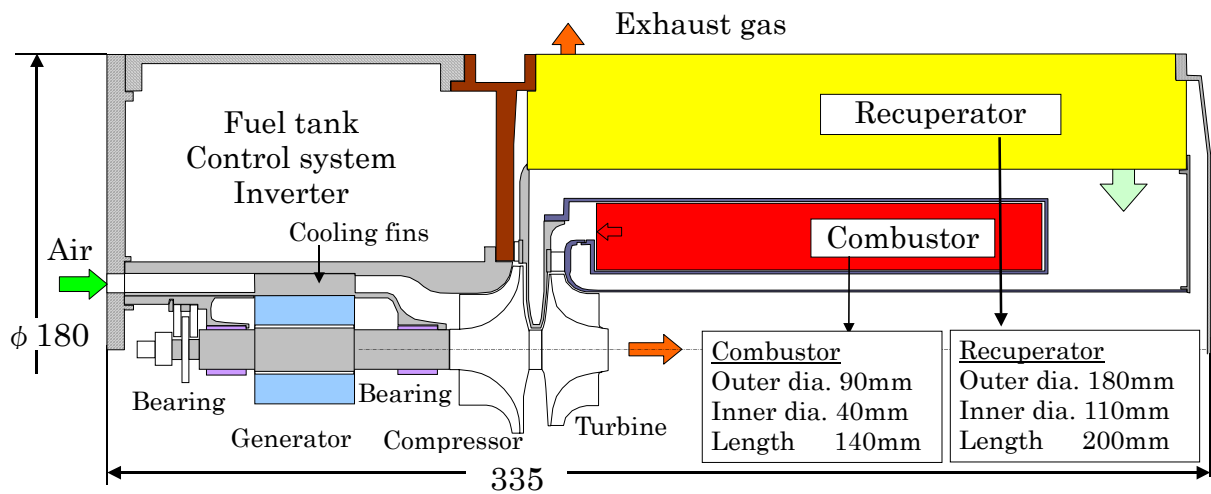
### 4.1 Design Particulars [2]

Design constraints were decided as follows:

- Capability of lubrication by either oil or gas bearings, since hydro-dynamic type of the latter with a shaft of 12mm in diameter has yet to be developed at the design speed of 235,000rpm;
- Critical frequency of the shaft vibration in the primary bending mode, lower than the frequency corresponding to the design speed of 235,000rpm;
- Bearings shielded from heat by combustion gas; and
- Compressor impeller protected from heat transfer as the best level.

#### 4.1.1 System Integration [2, 17]

Cut view and drawings of Palm-top gas turbine system are shown in Figure 6. A shaft, supported by a pair of bearings, passes all the way from the turbine rotor through the center of compressor impeller and generator rotor, and is fixed by means of a tension bolt to compose a unitary structure. Cooling fins are placed along the air path to the compressor to serve for cooling the generator stator, while a part of this suction air is diverted to cool the bearings and generator rotor. High pressure air exiting the compressor is fed to the regenerative heat exchanger, exchanges heat with the exhaust gas, and enters the combustor inner and outer periphery through air holes. The gas turbine unit is ready for assembly/disassembly by means of 24 bolts at the outer periphery of the casing.



Turbine bade diameter 40mm, Compressor wheel diameter 44mm,  
 Dry Weight 14.3kg, Volume 8.5 litter (8500 cc)

Figure 5: Plan of a Palm Top Gas Turbine.

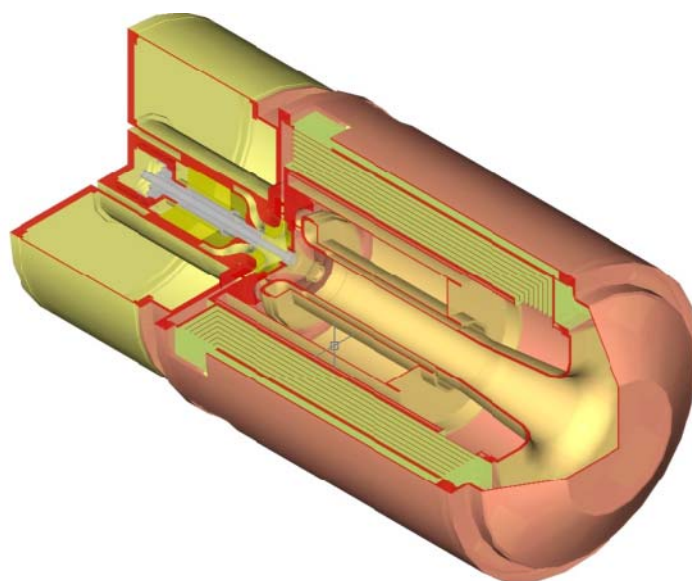


Figure 6: Sectional Drawing and Cut Model of Palm Top Gas Turbine.



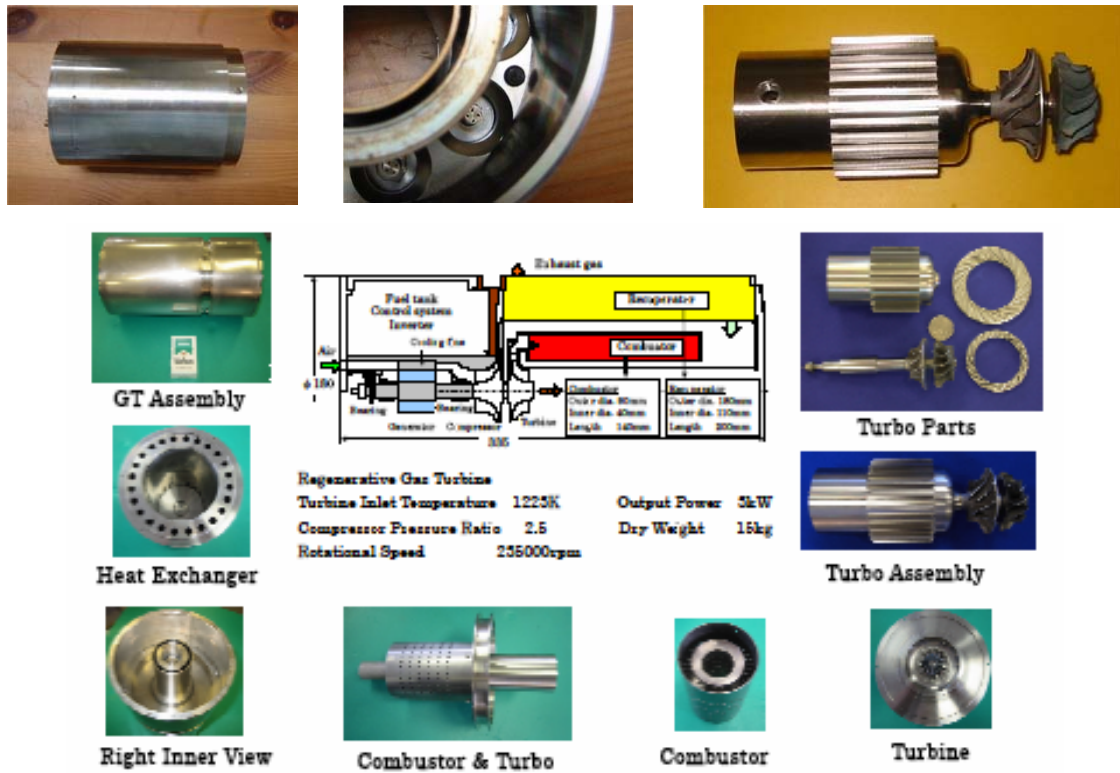


Figure 7: Components of a Palm Top Gas Turbine.

#### 4.1.2 Turbines [2, 19]

##### *Aerodynamic Design*

Table 4 and Figure 8 respectively show the specification of 2D designed turbines and the corresponding velocity triangles at the exits of nozzle and rotor. Degrees of reaction are 0.6, 0.74 and 0.47 for Model 1, Model 2 and Model 3 turbines, respectively. Model 2 was expected to attain peak efficiency at a relatively low velocity ratio  $u/C_0$  with some advantage for material stress reason, whilst, Model 3 turbine was designed in order to obtain a highest possible efficiency by applying a minimum possible nozzle-exit vane angle. The rotors and nozzles were made of aluminium as shown in figure 6, and cold air tests were performed to measure adiabatic efficiency.

Table 4: Specifications of Designed Two-Dimensional Turbines

	Model 1	Model 2	Model 3
Pressure ratio	2.91	2.91	2.91
Turbine Inlet Temp. [K]	1223	1223	1223
Rotational Speed [rpm]	$2.4 \times 10^5$	$1.9 \times 10^5$	$2.4 \times 10^5$
Mass Flow Rate [kg/s]	0.030	0.019	0.020
Nozzle Outer Dia. [mm]	52	52	52
Rotor Outer Dia. [mm]	40	40	40
No. of Blades (nozzle)	17	17	17
(rotor)	15	16	16
Blade Height [mm]	4.8	3.2	5.4
Output [kW]	7	4	5

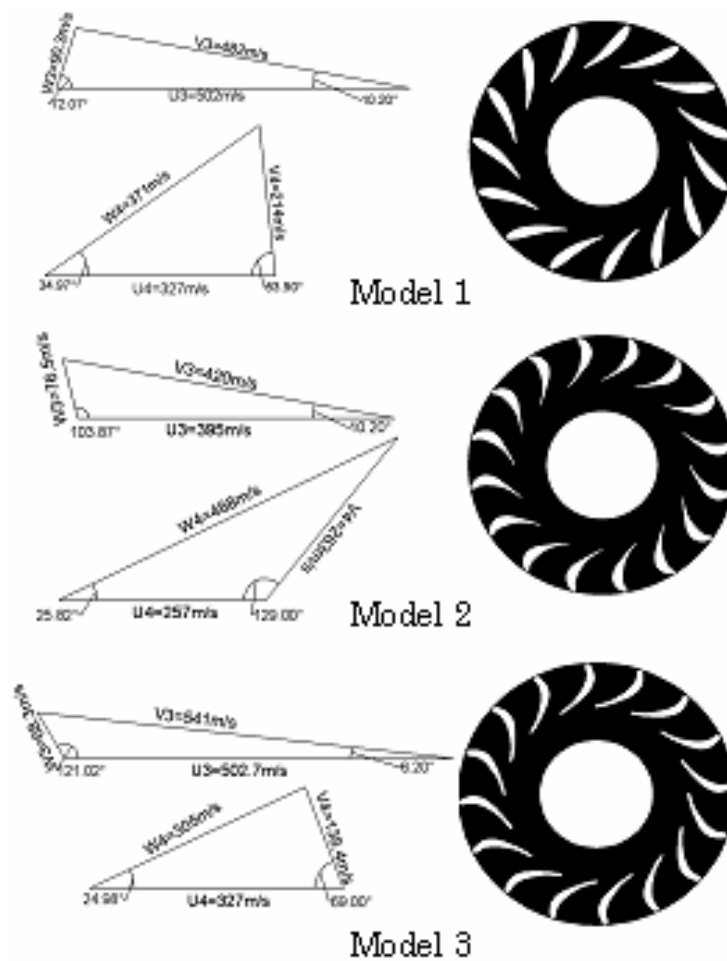


Figure 8: Velocity Triangles and Blade's Profiles of Designed Two-Dimensional Turbines.

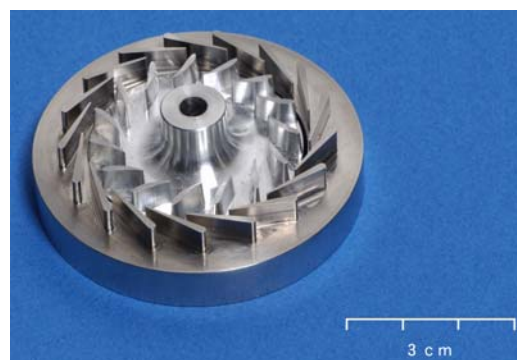
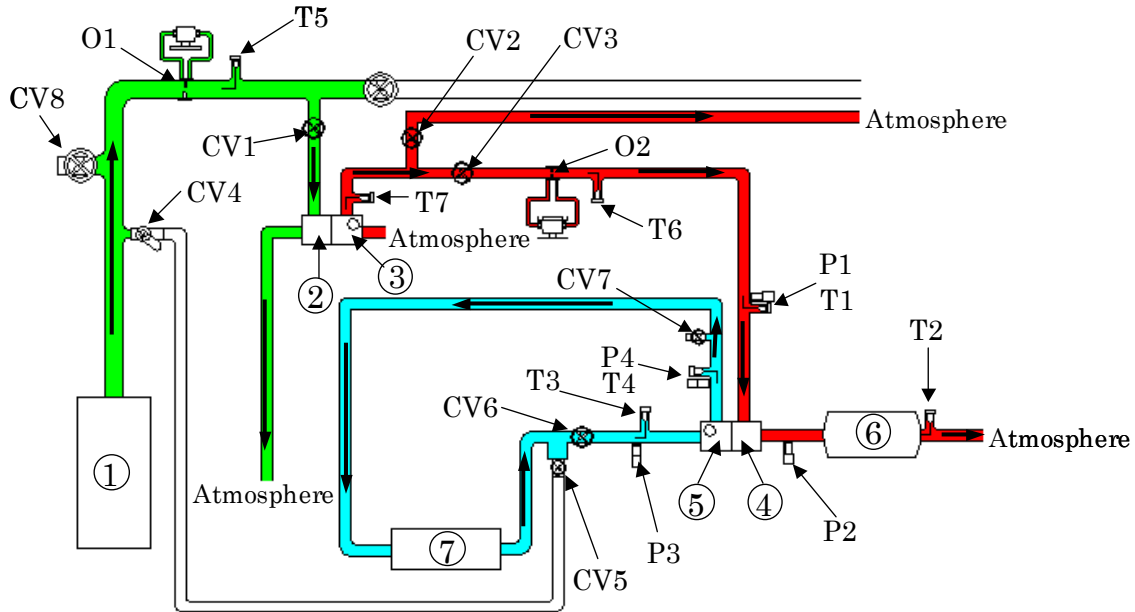


Figure 9: Fabricated Model 1 Turbine.

### Testing

The experimental facility is illustrated in Figure 10. Turbines<sup>④</sup> on test were driven by compressor discharge air<sup>③</sup> from a turbocharger <sup>②</sup>, which was needed to raise the air temperature into the test turbine for avoiding the ambient air dew reason. Air mass flow rate was measured by an orifice O2. Exhaust air

from a test turbine went into mixing chamber⑥, wherein temperature was measured at uniform condition. Turbine output was absorbed by a compressor⑤operating in a closed air loop that consists of air cooler ⑦ and control valves CV5-7 to adjust the loop mass flow rate and pressure for better control. The other measuring item was rotation speed.



- ①: Air Source
- ②: Turbine (Turbocharger)
- ③: Compressor (Turbocharger)
- ④: Turbine (Test Machine)
- ⑤: Compressor (Test Machine)
- ⑥: Mixing Chamber
- ⑦: Air cooler
- O1: Mass Flow Measuring Orifice (Turbocharger)
- O2: Mass Flow Measuring Orifice (Test Turbine)
- P1: Turbine Inlet Pressure
- P2: Turbine Outlet Pressure
- P3: Compressor Inlet Pressure
- P4: Compressor Outlet Pressure
- T1: Turbine Inlet Temperature
- T2: Turbine Outlet Temperature
- T3: Compressor Inlet Temperature
- T4: Compressor Outlet Temperature

Figure 10: Experimental Set Up.

Test conditions were set at turbine pressure ratios of 1.5, 2.0 and 2.4, and rotational speed was adjusted so as to obtain the velocity ratio between 0.3 and 0.6. Turbine adiabatic efficiency was calculated by measuring temperature and pressure at the test turbine inlet and outlet. The heat loss that affects the evaluated efficiencies was avoided as much as possible by attaching heat insulation material on the test turbine and mixing chamber, as shown in Figure 11.

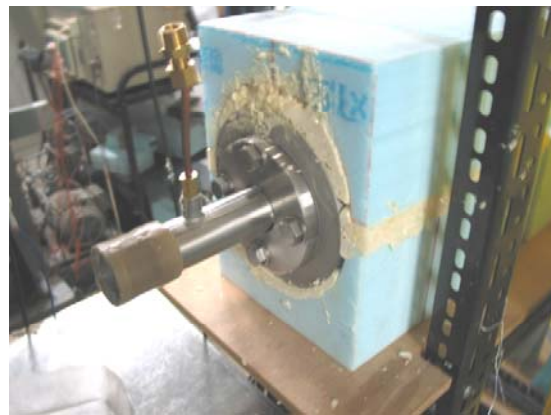
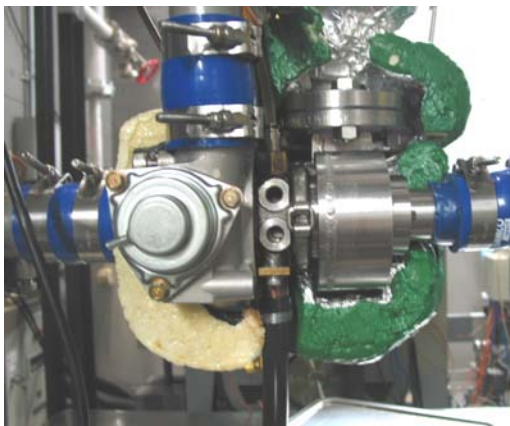
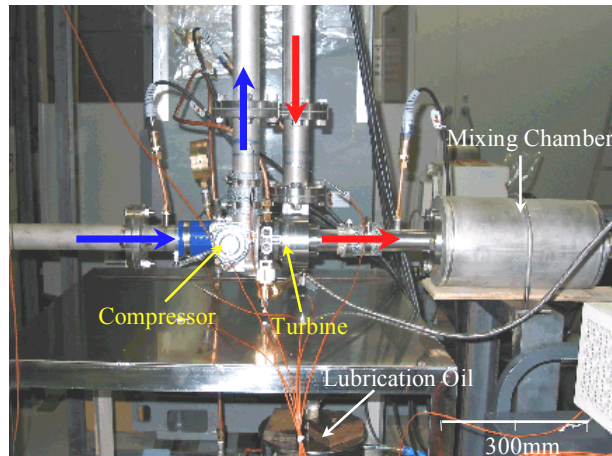


**Figure 11: Test Rig, (bottom)  
Close-up View: Compressor and Turbine (left) and Mixing Chamber (right).**

### *Preliminary Results*

Figure 12 shows the measured (heat loss compensated) adiabatic efficiencies versus the velocity ratio  $U/C_0$ . The number that follows “Pr” indicates the pressure ratio. CFD@Pr2.5 is a computational prediction at Pr =2.5 and “3D” means the measurements from 3D designed turbines that were also tested for comparisons. The numbers under each of the symbols indicate tip clearances in mm.

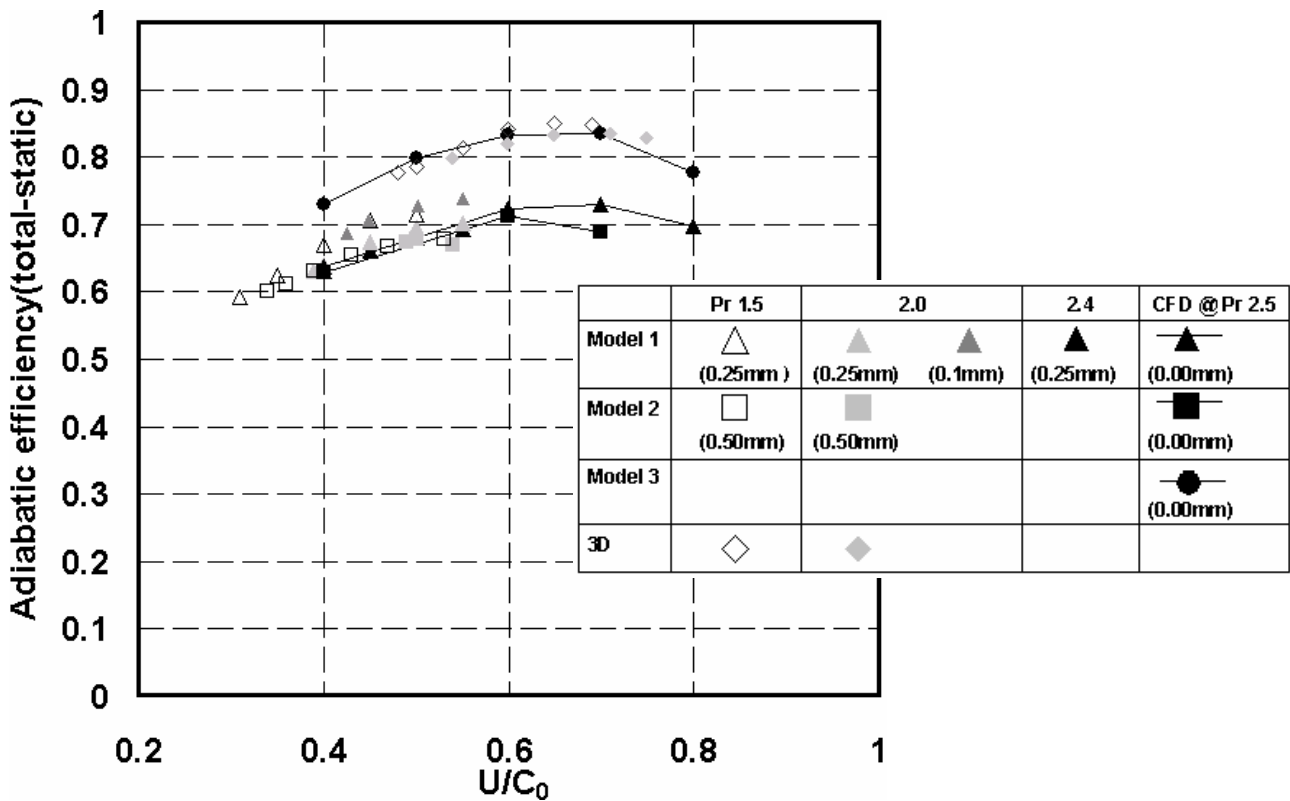


Figure 12: Measured Total-to-Static Adiabatic Efficiency.

The maximum adiabatic efficiency was 74% and 68% for Model 1 and Model 2, respectively. These efficiencies were at least 10% lower than that of 3D turbine, i.e. approximately 85%. Meanwhile, the tip clearance  $\delta$  considerably affected efficiency, for instance, increase from 0.1 mm to 0.25 mm resulted in approximately 4% reduction in the efficiency for Model 1 turbine. Since the blade height,  $b=4.8\text{mm}$ , a rule of thumb presently becomes expressed as: the loss in efficiency  $\sim 1.25(\delta/b)$ .

**Lesson:**

/In evaluating turbine adiabatic efficiency through the difference in total temperatures at inlet and outlet as presently, heat loss results in overestimation to a great extent. A preliminary test, despite insulation material, indicated that a 20 degree difference in ambient temperature resulted in as much as 4% difference in the measured efficiency as shown in Figure 13. In order to identify the major paths of heat loss, measurements were made at conditions in the absence of impeller rotation. Test results indicated that approximately 65% of the heat loss took place through the casing and mixing chamber and the remaining 35% through the bearings. Measured efficiencies were compensated based on the heat transfer coefficients and heat resistances that were thus determined by these preliminary tests. This resulted in an overall uncertainty of the measured adiabatic efficiencies within 2% independent of the ambient air temperatures.

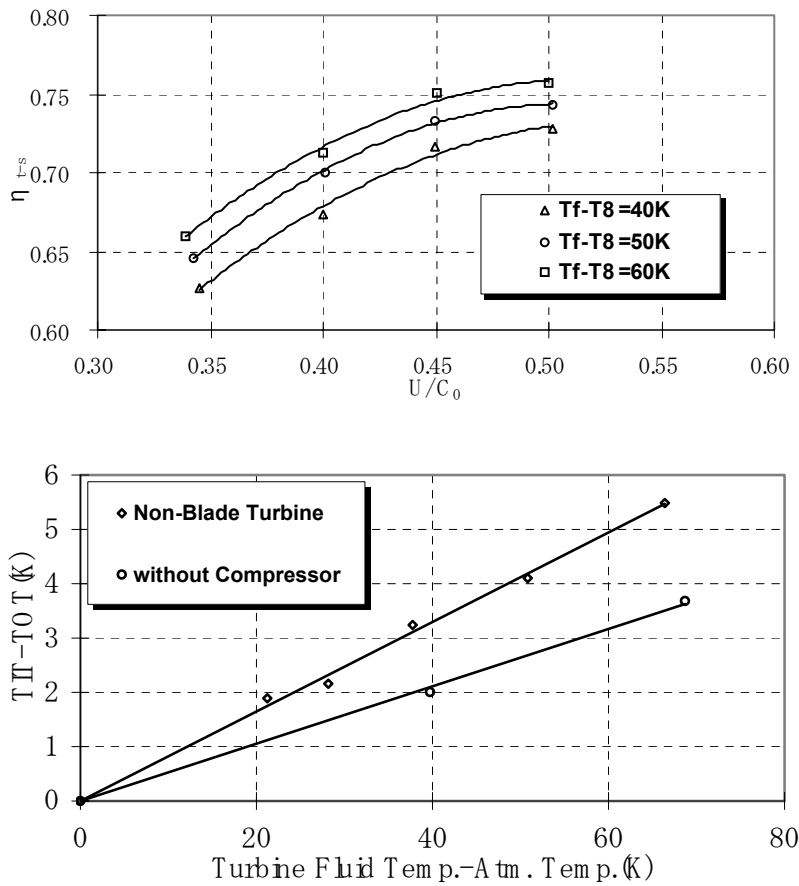


Figure 13: Preliminary Test Results showing Effects of Heat Loss on Measured Adiabatic Efficiencies.

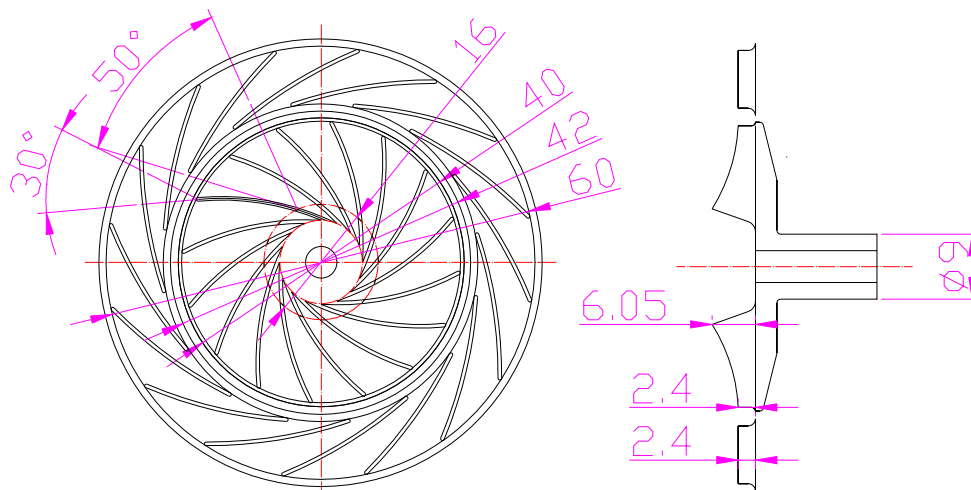
### 4.1.3 Compressors [2]

Design was made according to Galvas [20] geometry correlation for max. performance. Losses due to inducer incidence, wall friction, leakage, mixing and disc friction were examined, as well as diffuser blockage and pressure recovery coefficient were taken into account. Slip factor was calculated by Wiesner formula. Specifications of thus designed geometry are described in Table 5 and illustrated in Figure 14 below.

Table 5: Specification of Impeller and Diffuser

Impeller	Inlet diameter [mm]	16
	Exit diameter [mm]	40
	Number of blades	16
	Thickness of blades [mm]	0.5
	Inlet blade height [mm]	6.05
	Exit blade height [mm]	2.4
	Inlet blade angle [°]	50
	Exit blade angle [°]	30
Diffuser	Inlet diameter [mm]	42
	Exit diameter [mm]	60
	Number of blades	0,15,16
	Thickness of blades [mm]	0.5





All dimensions : mm

**Figure 14: Impeller and Diffuser.**

Design consideration is summarized as follows:

- Larger inlet diameter increases mass flow rate, but outlet flow angle from the impeller tends to increase flow angle towards decreasing pressure ratio. Inlet diameter was selected to be 16mm.
- Backward angle of impeller blade was decided 30 deg. by balancing between the larger loss due to increased kinetic energy and the increased mechanical stress due to centrifugal force.
- Number of impeller blades was determined to be 16. Larger number gives larger pressure ratio, but yields flow blockage leading to less mass flow rate at choke condition.
- Shorter diffuser is preferable for less friction loss, in accordance to the smaller size.
- Diffuser angle was chosen 10 deg. for the best flow stability, wherein incidence is about  $\pm 5$  deg.

Impeller was made from A7075. Across the blade span, blade thickness was 0.5mm except at its root of 1.0mm, and leading edge shape was curved, taking into consideration of sharp turning of the inlet flow. Diffuser, vaned or vaneless type, was made from brass. Two kinds of vanes diffuser were made with number of vanes 15 and 16, supported from the hub side into the flow passage with 0.3mm clearance to shroud wall. Impeller and diffusers are shown in Figure 15.

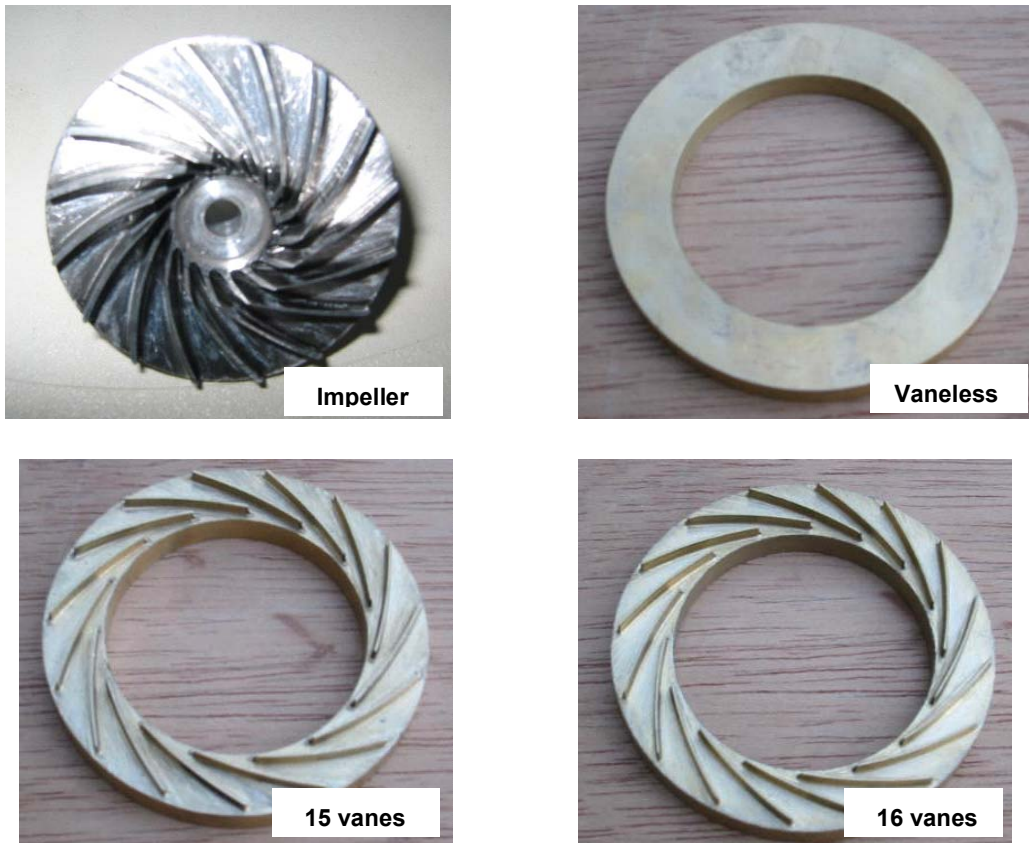


Figure 15: Impeller and Diffuser.

Measurements were carried out, at the impeller and diffuser exits, for temperature and static pressure, while static pressure and mass flow rate were taken at a station further downstream.

Compressor characteristics thus obtained are shown in Figure 16, with respect to 4 rotational speeds, up to the max. 110,000rpm so far, at which total pressure ratio was 1.65.

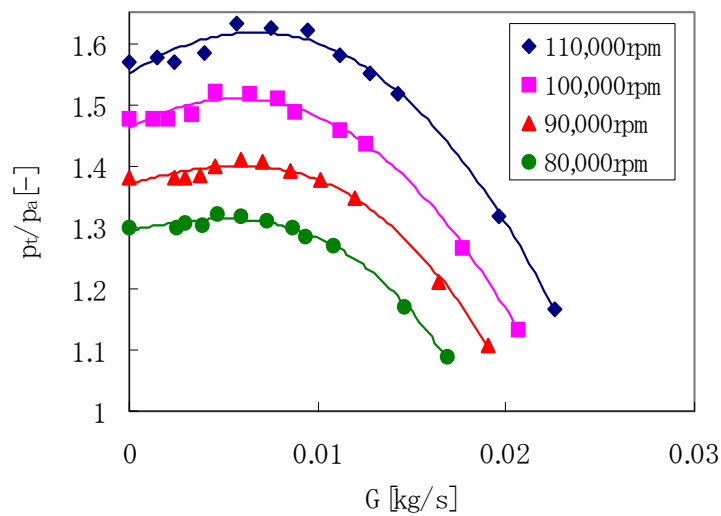


Figure 16: Preliminary Performance Results of Impeller+15 Vanes Diffuser.

Beside the aerodynamic performance, FEM stress analysis was also carried out to find impeller critical vibration modes and the corresponding frequencies to check the mechanical safety of the present impeller.

#### 4.1.4 Combustor [21, 22]

##### *Design Specifications*

Propane, instead of hydrogen, was chosen as fuel, because of considerable conventional use as well as due to its high vapour pressure at atmospheric temperature. To match Palm-top, the design specifications were as follows:

- Pressure ratio: 2.6
- Turbine inlet temperature: 950°C
- Air mass flow rate: 30 g/s
- Total pressure loss: 3 %

Combustor inlet temperature and equivalence ratio of propane/air were estimated to be 200C and 0.3, respectively. Of designing importance, presently, was the structure and size to match the recuperator employed, so that the exhaust gas path was made inner of the combustor, then through the recuperator set surrounding outer of the latter. In order to use the available space most effectively, preliminary design of a propane-fuel annular micro combustor (inner diameter 50 mm, outer diameter 98 mm, length 100 mm) was made. The volume of the combustor was determined to achieve high space heating rate (*SHR*) of 180 MW/(m<sup>3</sup>·MPa) at the design point. Flame stability was ensured by eight small flames placed in annular so as to maximize the area of air-inlet nozzle, reducing air flow velocity to the minimum there. Power output per each fuel injector amounted to a 300-W class power generator.

##### *Single-Can Type Combustor*

A single-can type combustor, simulating one of 8 flames in the full scale annular micro combustor in proposal, was prepared to examine its combustion characteristics. Figure 17 shows the test model installing a fuel injector and a set of air-inlet swirler and nozzle. Various types of the injectors and air-inlet nozzles shown in Figure 18 were tested to examine the effect of diameter and number of fuel injection holes as well as throat diameter of air-inlet nozzle upon the combustion characteristics. Air entered into the chamber of 46 cm<sup>3</sup> in volume through radial flow-type swirler and air-inlet nozzle. The geometrical swirl number was set 3.0. Propane fuel was injected with a swirl in the same direction as air flow by the injector with 4 or 6 injection holes. The test model had a quartz wall without secondary air holes. When measuring ignition limits, the latter was replaced by stainless steel wall, installing an electrical spark igniter at the flame impinging position of 10 mm downstream from the injector. The present experiment was carried out without preheating the air and at atmospheric pressure. Therefore, the air flow rate needed reduction for Palm-top design point operation, i.e. to the air mass flow rate  $m_a$  of 2.56 g/s.

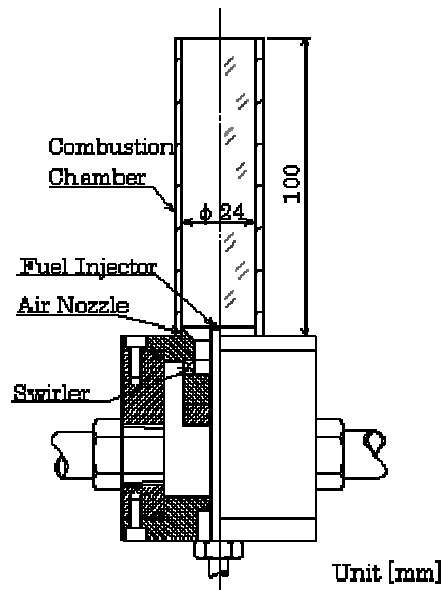
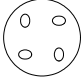
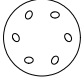
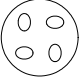


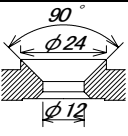
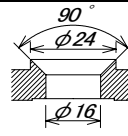
Figure 17: Schematic of Test Single-Can Combustor.

Fuel injectors

Diameter of holes	0.6 mm	0.5 mm	0.8 mm
Number of holes	4	6	4
Type	$\phi 0.6 \times 4$ type	$\phi 0.5 \times 6$ type	$\phi 0.8 \times 4$ type
Cross section			
Holes area	1.6 mm <sup>2</sup> ( $U_f=16.8$ m/s)	1.7 mm <sup>2</sup> ( $U_f=16.1$ m/s)	2.8 mm <sup>2</sup> ( $U_f=9.5$ m/s)

※ $U_f$  : Fuel injection velocity at  $\phi=0.3$

• Air-inlet nozzles

Throat diameter	12 mm	16 mm
Type	$\phi 12$ Nozzle	$\phi 16$ Nozzle
Cross Section		
Throat area	93 mm <sup>2</sup> ( $U_a=24$ m/s)	181 mm <sup>2</sup> ( $U_a=12$ m/s)

※ $U_a$  : Air injection velocity at design point

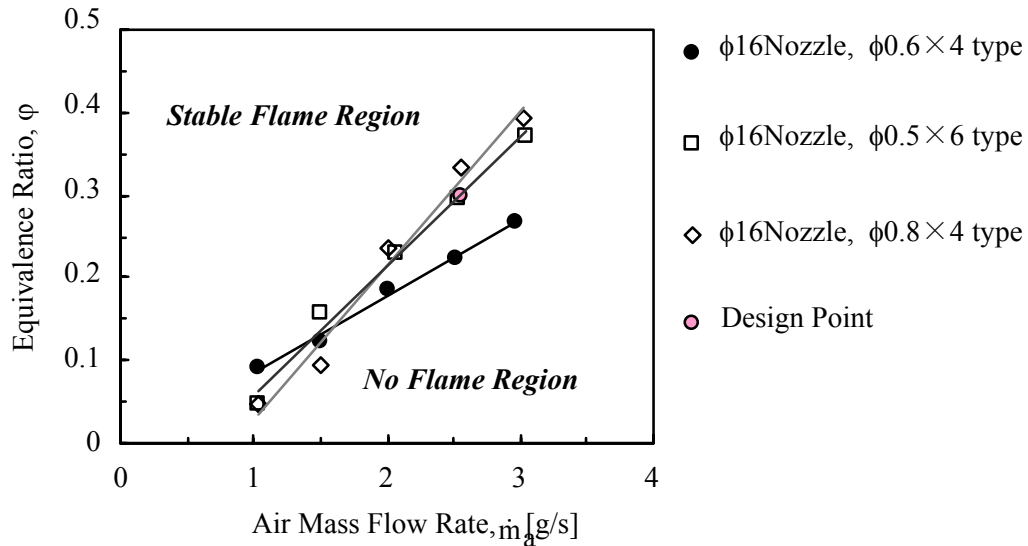
Figure 18: Schematic of Fuel Injectors and Air-Inlet Nozzles.

Combustion Characteristics

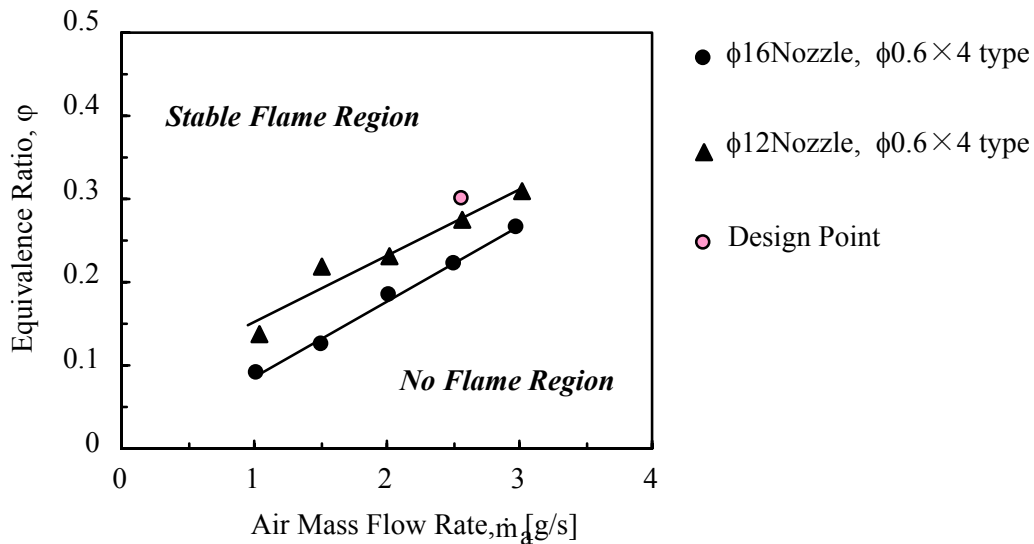
1) Flame Stability Limits and Ignition Limits:

Figure 19 shows the flame stability limits for (a) three injector sizes and (b) two air-inlet nozzles. For all the injectors and nozzles, blow-off limits increased by increasing the air flow rate. In cases of  $\phi 16$  nozzle,

the type of  $\phi 0.6 \times 4$  injector only satisfied the flame stability region at the design point, which is due to that, for the other types, high temperature gas met more difficulty in recirculation through the interval between the fuel holes. While, by employing  $\phi 0.6 \times 4$  type injector,  $\phi 16$  nozzle exceeded  $\phi 12$  nozzle, which can be explained by that, for the larger nozzle, flow velocity at the nozzle exit got slower, thus the high temperature recirculation region developing in the swirling air stream easily expanded upstream beyond the injector exit. Meanwhile, Figure 20 shows the electrically ignition limits. It was found that ignition occurred at the region of much larger equivalence than the blow-off limits.



(a) Effect of fuel injectors



(b) Effect of air-inlet nozzles

Figure 19: Flame Stability Limits.

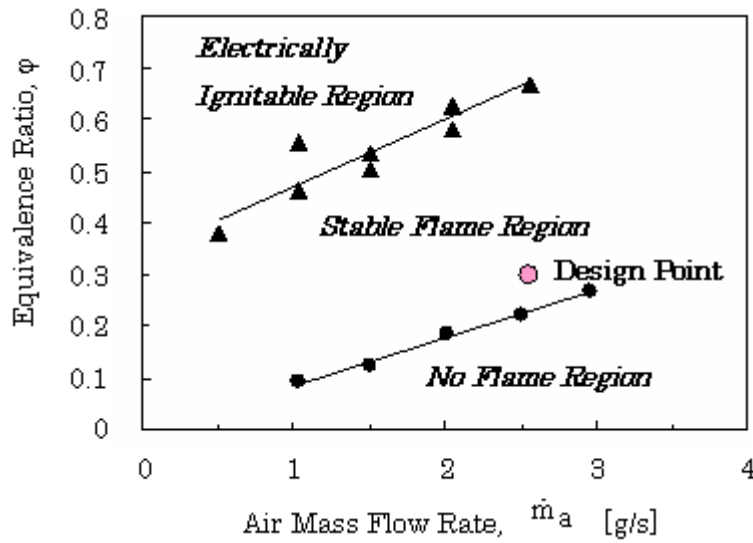


Figure 20: Flame Stability Limit and Electrically Ignition Limit.

## 2) Flame Appearances

Figure 21 shows variations in flame appearance corresponding to different combinations of air-inlet nozzle and fuel injectors. Flames were sufficiently inside the combustor, indicating that space heating rate remained extremely high at the design point. Depending on injectors, flame lengths shown in (c) and (d) were slightly shorter and paler in colour than in (b), wherein flames in (c) and (d) emitted an offensive odour. This suggests unburned fuel exhaust due to incomplete combustion. By employing different nozzles, the flame length was shorter in (a) than (b), which seemed for reason that the air flow passing through the narrower nozzle exit, thus with more speed, can spread wider due to strong swirl that caused rapid progress in combustion due to strengthened turbulent mixing with the fuel jets.

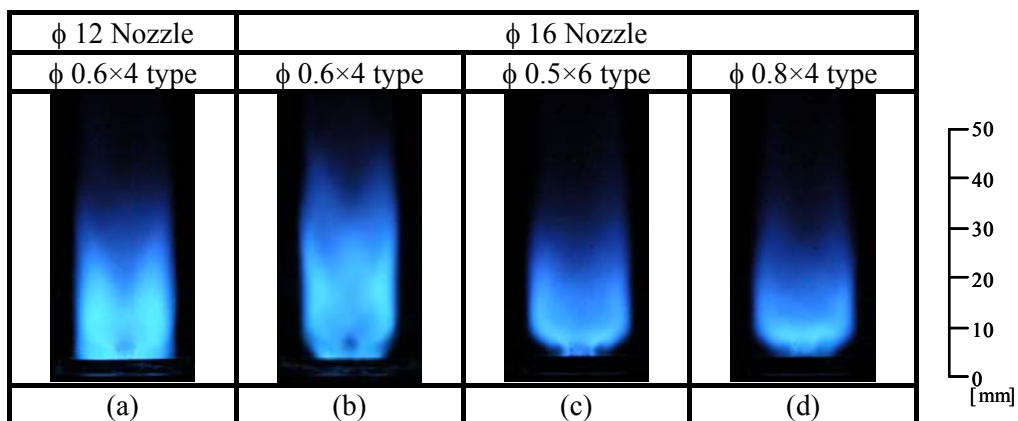


Figure 21: Flame Appearances ( $m_a = 2.56\text{g/s}$ ,  $\phi = 0.4$ ).

## 3) Temperature Distribution

Figure 22 shows an example of the temperature distributions in a test employing  $\phi 0.6 \times 4$  type injector with nozzles of both  $\phi 12$  and  $\phi 16$ , at the design point. Recirculation zone boundary confirmed by Na flame reaction is also shown. Measured temperatures are without correction for radiation and conduction losses.



Comparison between the temperature distributions and the flame configurations indicated that the flame front coincided with the isotherm of about 1200C. Airflow field surrounding the propane injector played a crucial role in determination of flame behaviour because of the larger air flow momentum as a whole. With  $\phi 12$  nozzle, flame spread close to the combustor wall, corresponding to the wide recirculation region. However, the high temperature region over 1200C did not expand on the fuel injection plane, wherein lifted propane jet flames were observed to form near the injector exit. On the other hand, with  $\phi 16$  nozzle, shape of the recirculation region was long and narrow, temperature near the centre axis was higher and the high temperature recirculation zone further expanded beyond the fuel injector exit. The flame base was thus anchored in the recirculation region, leading to an excellence in flame stability as shown in Figure 19. These results also indicated that flow near the wall seldom participated in combustion.

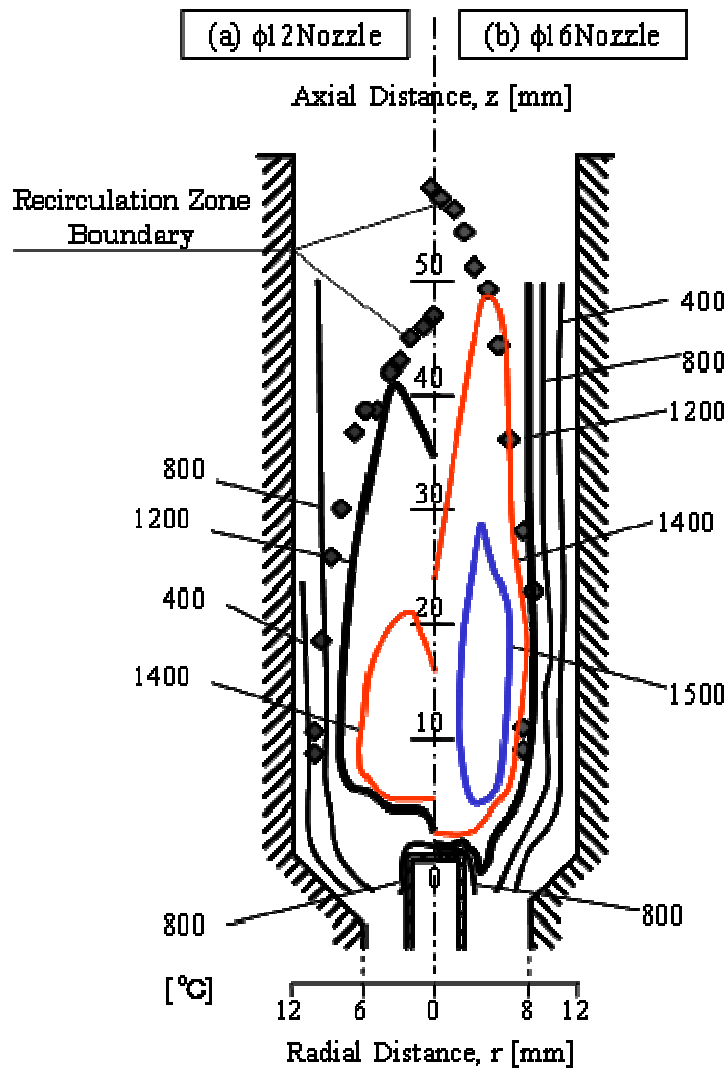


Figure 22: Temperature Distributions in the Test Combustor in a Horizontal Plane ( $\phi 0.6 \times 4$  type,  $m_a = 2.56 \text{ g/s}$ ,  $\phi = 0.4$ ).

#### 4) Temperature Distributions and CO Concentrations at the Combustor Exit

Figure 23 shows temperature distributions and CO concentrations at the combustor exit at the design point. For both types of nozzle, the exit temperature distribution was not uniform, corresponding well to the results shown in Figure 21, which indicates dominant effect of the flame on the exit temperature.

CO concentration was extremely low at the central part where temperatures were high, while increased suddenly near the combustor wall. Meanwhile, CO concentration near the wall was lower for  $\phi 16$  nozzle than  $\phi 12$  nozzle. This may be explained by that, for  $\phi 16$  nozzle, high temperature near the central axis made injected fuel burnt almost completely there, achieving high enough combustion efficiency, in contrast with the flame for  $\phi 12$  nozzle that expanded close to the wall and quenched due to severe heat losses, resulting in increased CO concentration.

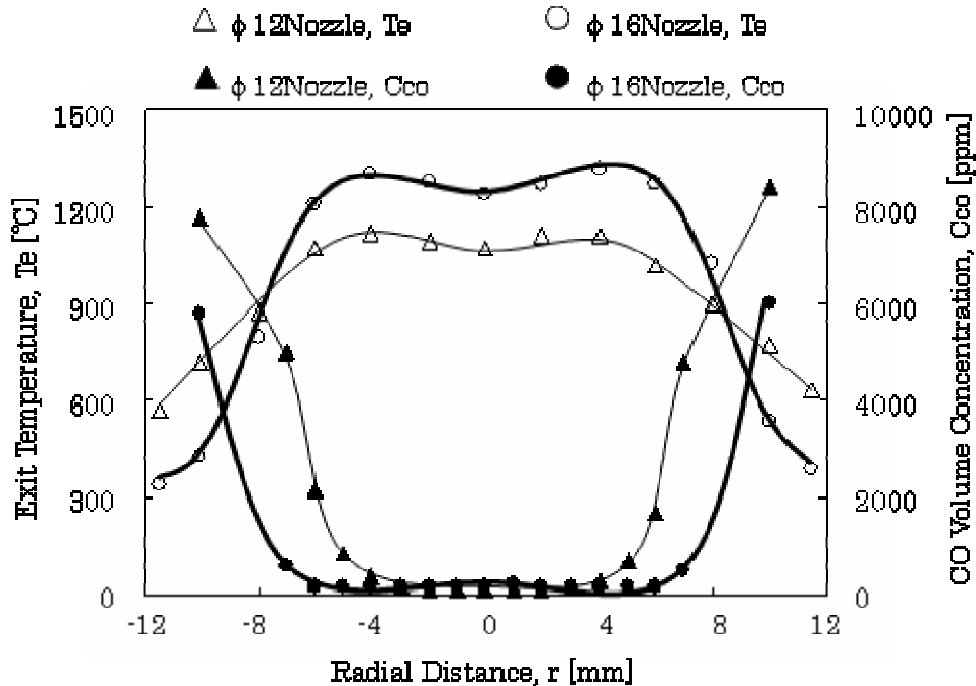


Figure 23: Temperature and CO Concentration at the Combustor Exit ( $\phi 0.6 \times 4$  type,  $m_a = 2.56 \text{ g/s}$ ,  $\phi = 0.4$ ).

##### 5) Total Pressure Loss Ratio

The total pressure loss ratio, defined as  $PL \equiv \Delta P / P_c$  ( $\Delta P$  : total pressure drop across the combustor,  $P_c$  : combustor inlet pressure), was 1.2% for  $\phi 16$  nozzle, while 1.9% for  $\phi 12$  nozzle, at design air flow rate of 2.56 g/s. Both were lower than the target value of 3% for Palm-top.

##### Prototype Annular MicroCombustor

Upon selecting the combination of  $\phi 0.6 \times 4$  type injector and  $\phi 16$  air-inlet nozzle for better flame stability and less CO exhaust, a prototype annular micro combustor was designed as shown in Figure 24. Aiming for miniaturization with a simplest structure and judging also that wall can endure the temperature level found in experiments, secondary air holes were not employed. Pressure loss ratio was estimated as about 1.7%, and space heating rate was  $180 \text{ MW}/(\text{m}^3 \cdot \text{MPa})$  at the design point.

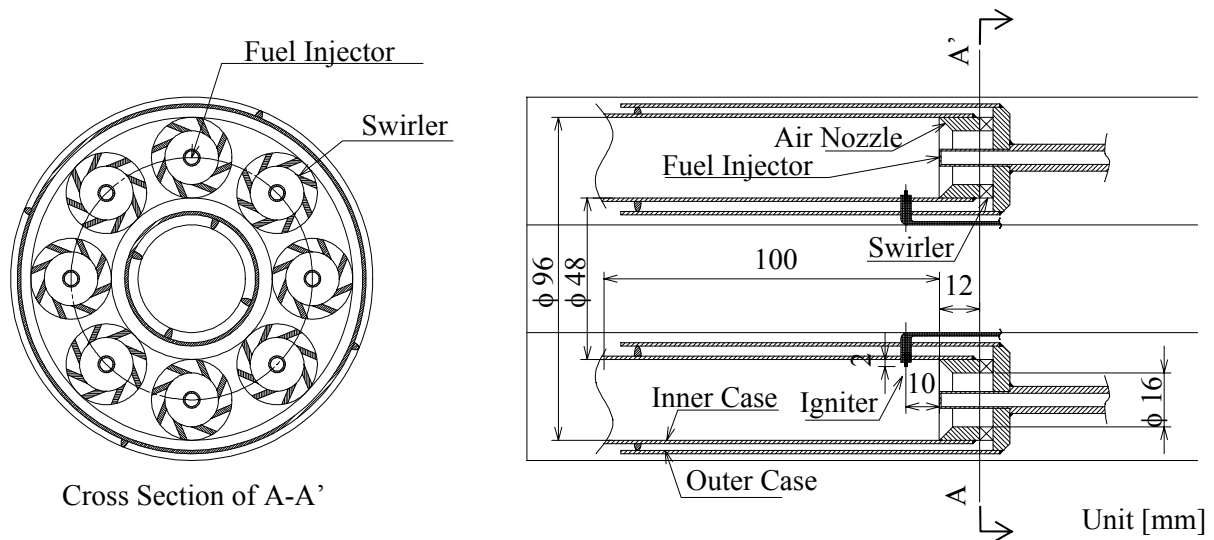


Figure 24: Design of Prototype Annular Micro Combustor for the Palmtop Gas Turbine.

### Lessons:

/Lower air-inlet velocity and stronger swirl increase flame stability of propane jet diffusion flames in a swirling air flow confined in a small combustion volume.

/When a strong recirculation region is developed near the fuel injector exit, flame stability increased with a decrease in diameter and number of fuel injection holes.

/High temperature recirculation gas passing through the intervals between fuel injection holes plays a crucial role on flame stability.

/Combination of the fuel injector with a wide interval of fuel injection holes and the air-inlet nozzle with a large throat diameter is excellent in flame stability, space heating rate and combustion efficiency.

### 4.1.5 Bearings and Rotor Dynamics [24-29]

The foil bearing under study may be called as ‘multi wounded type radial foil bearing’, which is easy for fabrication and assembling as well as mathematical modelling, therefore, has been adopted as radial bearings and spiral groove bearings for a thrust bearing.

#### *Construction and Dimensions of Rotor*

The rotor structure used in experiments is shown in Figure 25. The rotating shaft consists of the following four parts, the rotor with turbine, a sleeve, a thrust disk, and a nut for fixing the thrust disk to the rotor. The stainless steel (SUS402J2) was used for the sleeve, and the surface is coated by ceramic. At the right end of the rotating shaft, a reverse thread was cut in order to fix the thrust disk, and a through hole was pierced for measuring the rotational speed. The sleeve was inserted under pressure and fixed to the shaft. The diameter of the sleeve, the length of the rotor, total weight of the rotor are 20mm, 190mm and 0.5kg, respectively.

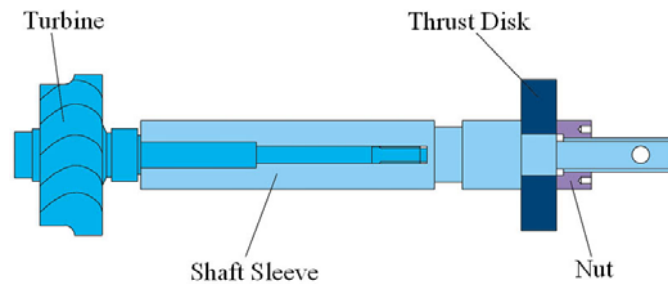


**Figure 25: Rotor Assembly.**

*Construction and Dimensions of Radial Bearings and Thrust Bearings*

The layout of the manufactured radial foil bearing is shown in Figure 26. This bearing is composed of the housing and a multi wound foil with hemispherical projections placed on one side at an adequate position. The foil is made from a phosphor bronze plate of 0.1mm in thickness, 20mm in width, 202mm in length, and has 160 hemispherical projections, the height of which is 0.2mm (Figure 27). In assembling as the radial foil bearing, first, the plate was bent at the position 3mm apart from the edge, and then, embedded in the slot of the housing. Then, the foil was wound spirally and fixed with the housing. Due to the rotation of the shaft, a wedge like space is formed between the shaft and the bearing surface. Presently, the bearing radial clearance between axial surface and bearing surface is  $20\ \mu\text{m}$ , because the foil is triply wounded.

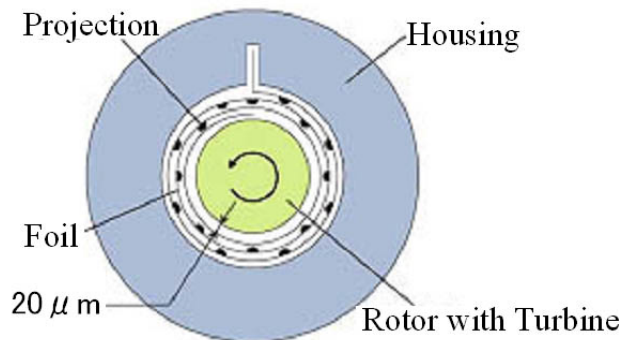


**Figure 26: Schematic View of Foil Bearing.**

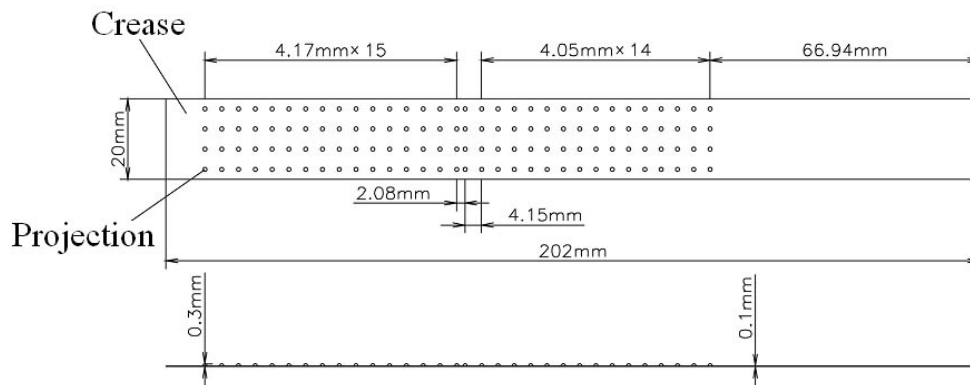


**Figure 27: Dimensions of a Foil and Projections.**

Thrust bearings used in this experiment are spiral groove thrust bearings with 0.5kg load capacity designed in accordance with the regular design procedure (Figure 28).

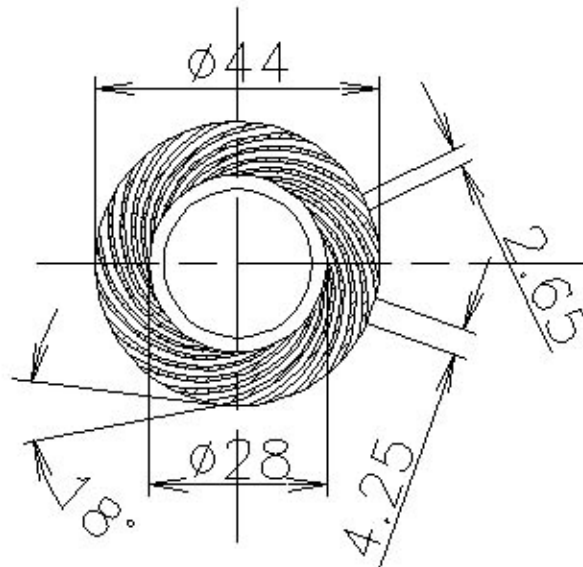


Figure 28: Major Dimensions of Thrust Bearing.

*Test Rig for Measuring Bearing Characteristics*

In Figure 29, the schematic view of the apparatus for measuring bearing static and dynamic characteristics is shown. During the measurement, the rotor is driven by compressed air supplied from compressor through the scroll. Measurements were made for rotational speed and lateral, conical and axial motion of a rotational shaft by using optical fiber sensor and eddy current type displacement sensors, respectively.

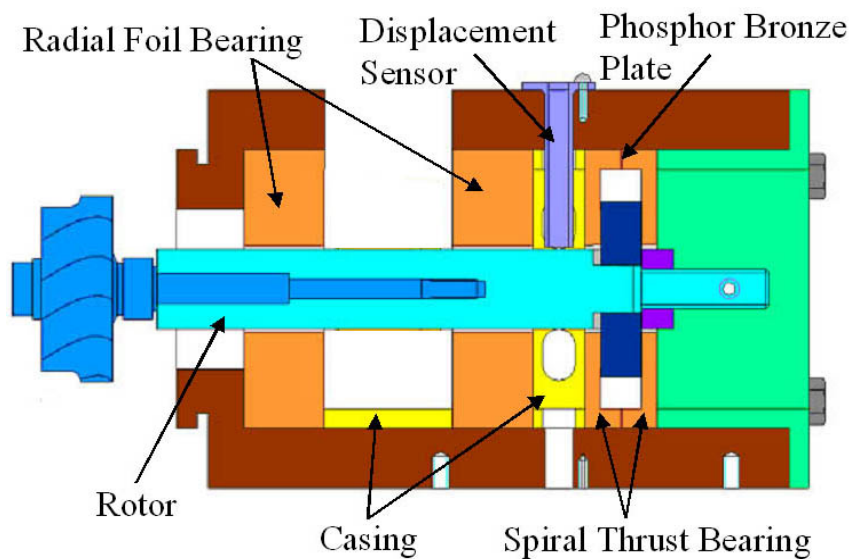
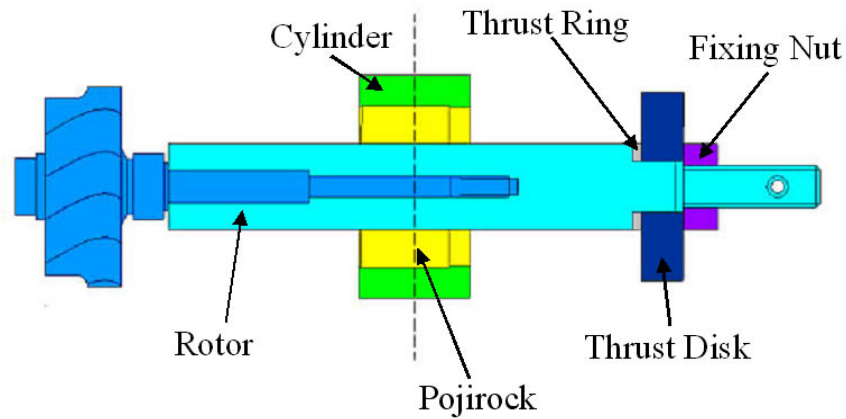


Figure 29: Test Rig for Measuring Bearing Characteristics.

*Load Capacity Test*

In testing, a pojirock was equipped in the middle of the rotating shaft as a load variable element as shown in Figure 30 to investigate the load capacity characteristics.



**Figure 30: Rotating Shaft for Load Capacity Test.**

Test results of load capacity are summarized in Figure 31 as a function of eccentricity and rotational speed as a parameter.

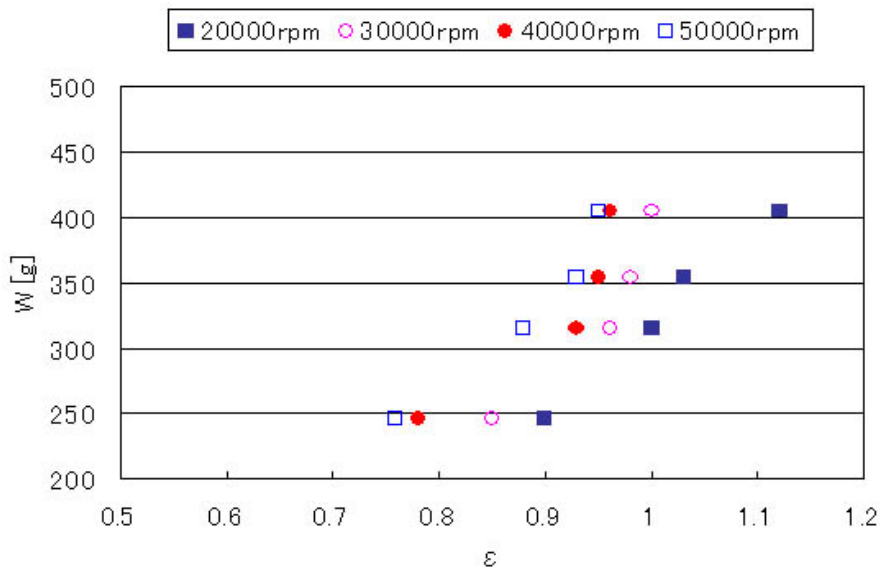


**Figure 31: Load Capacity Characteristics.**

In what follows, typical experimental data are summarized. In Figure 32 and Figure 33, vibration data when the rotational speed is 50000rpm and turbine inlet pressure is 8.3kPa are shown.



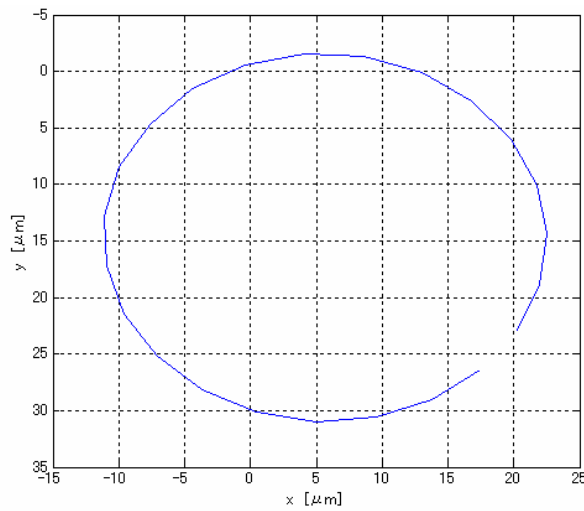


Figure 32: Lissajous Figure.

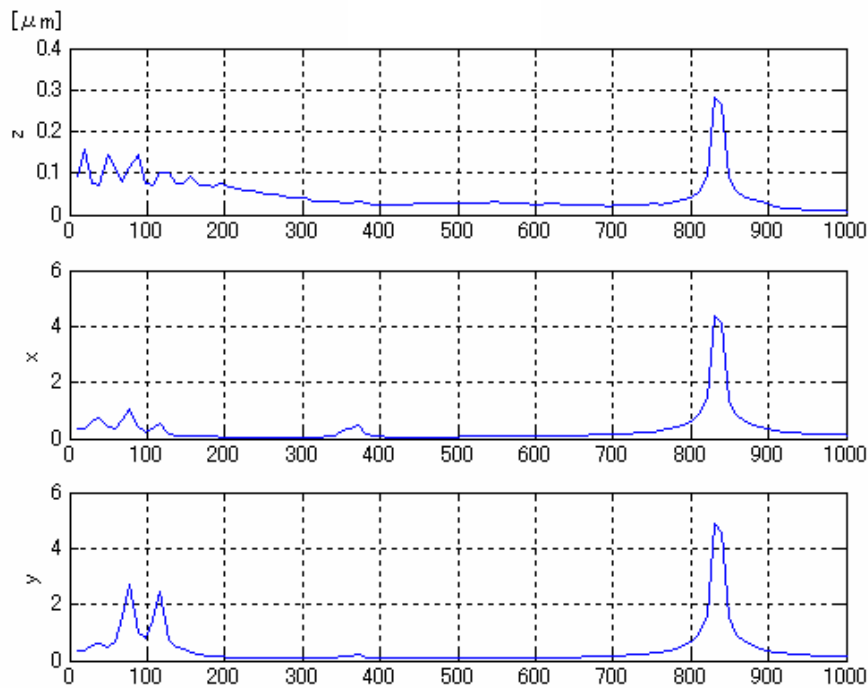


Figure 33: Frequency Spectra of Vibrational Data for x, y, z Axes.

#### 4.1.6 Heat Exchanger [2, 30, 31]

Based upon well established and reliable manufacturing technology, a plate-fin recuperator with offset strips was selected. The currently finest fin available for this type may be of size like  $Wf=1.02\text{mm}$ ,  $Hf=3.2\text{mm}$ ,  $Lf=3.2\text{mm}$ ,  $\delta f=0.1\text{mm}$ ,  $\delta w=0.3\text{mm}$ .

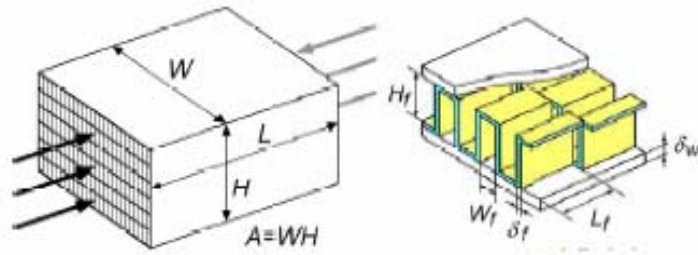


Figure 34: Definition of Recuperator and Offset Strip Fin Size.

The performance is evaluated by effectiveness,  $\epsilon$ , defined by a ratio between the temperature differences:

$$\epsilon = \frac{T_{a,out} - T_{a,in}}{T_{h,in} - T_{a,in}}$$

As a component of gas turbine system, it is important to achieve higher effectiveness at less pressure loss, which however requires generally a larger volume as shown in Figure 35.

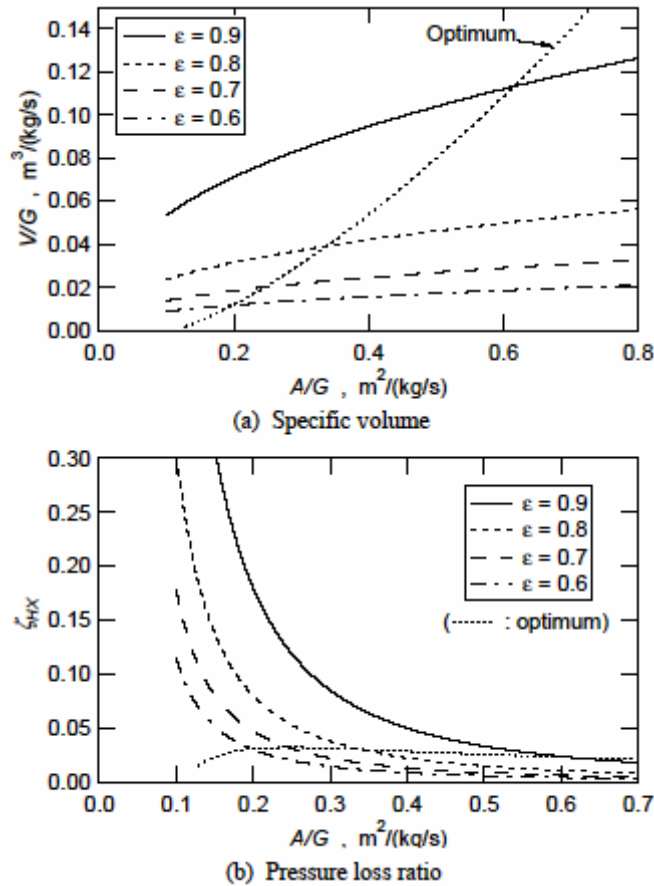


Figure 35: Variation of Recuperator Size and Pressure Loss with Specific Frontal Area at Constant Effectiveness.

Sharp increase of the pressure loss is noticeable as the abscissa gets smaller, meaning larger mass flux or velocity. Compactness of this type of recuperator therefore has to be negotiated with respect to not only the effectiveness but also the pressure loss, both yielding a significant influence upon the thermal efficiency of a gas turbine system.

Presently, a configuration shown in Figure 36 was designed, which consists of 8 box type recuperator units in annular arrangement surrounding the turbine, so that it can eliminate the duct extension, reduce the heat loss out of the combustor and minimize the overall turbo package size. (Target weight was under 6 kg, but it actually was 8.2 kg. See Palm-top GT general view.)

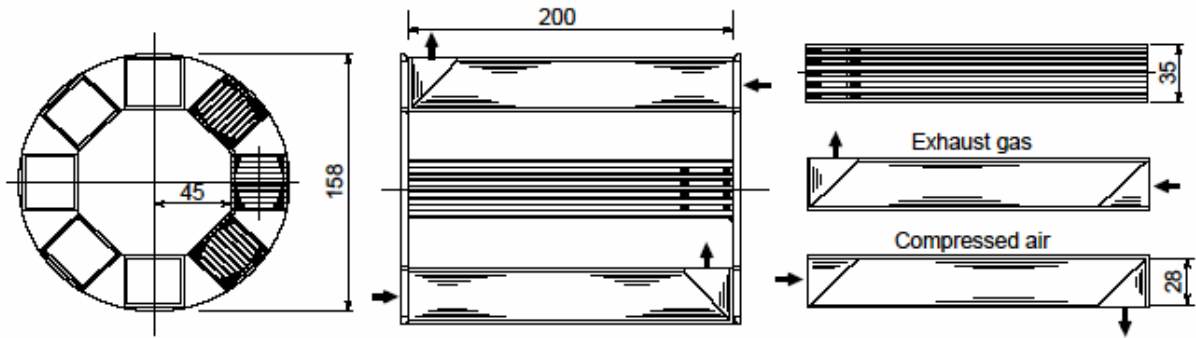


Figure 36: Designed Recuperator for 3kW GT ( $\epsilon=0.8$ ).



Figure 37: Picture of Manufactured Recuperator.

The total volume of matrix core is 1,186 cm<sup>3</sup>, giving the volume/mass flow rate of 0.040 m<sup>3</sup>/(kg/s) and the predicted effectiveness is 0.8. Leading specifications of the palm-top GT, including the performance prediction, are listed in Table 6. A substantial improvement of thermal efficiency from 14.4% to 28.5% can be achieved, though power output is slightly deteriorated from 3.66kW to 3.24kW.

Table 6: Specification and Performance of Postulated 3kW Class Micro Gas Turbine

Gas flow rate	0.03 kg/s
Turbine inlet temp.	1223 K
Pressure reatio	3
Turbine efficiency	0.8
Compressor efficiency	0.75
Combustor pressure loss	3 %
Without recuperator	
Power output	3.66 kW
Efficiency	14.4 %
With the present recuperator	
Effectiveness of recuperator	0.8
Pressure loss of recuperator	6.3 %
Power output	3.24 kW
Efficiency	28.5 %

**Lessons:**

/The benefit of recuperator heat recovery can be easily cancel out by pressure loss increase due to installation. Figure 38 shows thermal efficiency against specific volume at constant effectiveness. Curves tend to give rapid rise and then asymptotic values in efficiency as volume increases, in other words, less pressure loss. Whilst, at a given volume, efficiency increases as effectiveness gets the higher, however, up to a value beyond which efficiency starts to decline because of associated rapid increase of pressure loss. Therefore, there is an optimum effectiveness at each recuperator volume. The optimum points thus obtained are also plotted in Figure 35a,b as a dotted curve “Optimum”.

/The present design yielding effectiveness of 0.8 with specific volume of 0.04 corresponds to a point close to the optimum condition, though slightly shifted to the more compact type. This shift affects little in efficiency due to the latter stationary behaviour around the optimum condition (Figure 6).

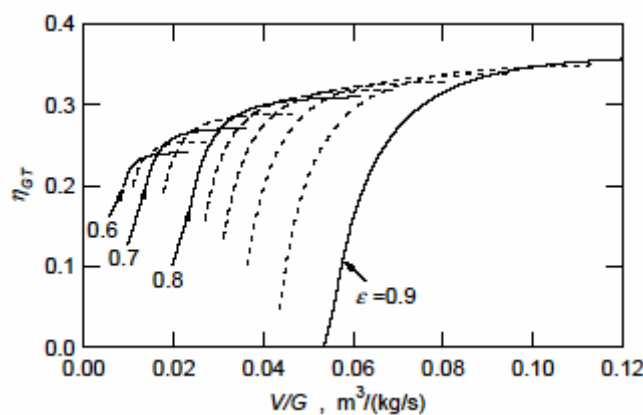


**Figure 38: Relationship between Cycle Thermal Efficiency and Recuperator Specific Volume at Constant Effectiveness.**

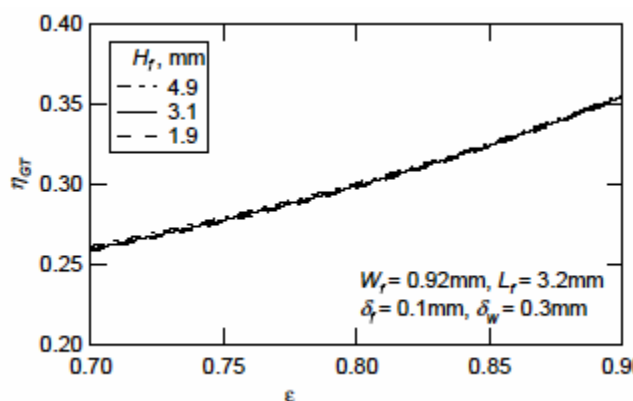


**Figure 39: Relationship between Cycle Thermal Efficiency and Recuperator Effectiveness at Optimum (minimum volume) Point.**

**4.1.7 Electric Motor-Generator [2]**

Between two representative types of magnetic and electrostatic induction, there is very few electrostatic motor-generator products in the market. The reason is due to overwhelming difference in the maximum obtainable energy density across a distance of mm at atmospheric condition. Permanent magnet type was thus selected for Palm-top with an internal neosium magnet placed inside the rotor and a newly developed

silicon-embedded type ultra thin magnetic plate in the stator. A test motor of 5kW output was fabricated, and motor tests were conducted to achieve 180krpm using a centrifugal compressor as a dynamometer. Stable operation was confirmed at up to 160krpm, but damage to the windings (thought to be due to over-current) occurred at 180krpm. Accordingly, the design is being reexamined, including the sensor-less control. Installation of this motor-generator to Palm-top was already described in the previous general view, such that the centre single shaft originated from the turbine rotor acts as a long tension bolt going all through the compressor rotor, motor-generator rotor and gas bearings. The motor-generator stator is cooled by fins, whilst its rotor and the bearings are directly cooled by air, upstream of the compressor inlet. Some 30~40% of design speed (70k~94krpm) is sufficient for starting motors, so that tests were undertaken mainly as a generator. Development is required for lightweight compact frequency converters capable of converting, for a starter motor, 50/60Hz electricity into 400W at 1.2~1.6kHz and several W at 6.9~7.8kHz, while for a high speed generator, high frequency sinusoidal waveforms of 3kW at 3.9kHz or tens of W at 19.5kHz into direct current electricity. Accordingly, high speed rotational testing is being conducted to attain full controllability.



**Figure 40: Motor-States Rig.**

## 4.2 CFD Predictions [2, 32]

### 4.2.1 CIAM Profiles

CIAM proposed their original profiles, with predictions of performance for both compressor and turbine according to their numerical simulation results, which is explained in the next.

For compressor, the design pressure ratio was 3 at rotor speed of 210,000 rpm. The specifications are listed below. Blade tip clearance effects (leakage and friction) were not taken into account. Main conclusion was that their design can achieve adiabatic efficiency around 0.69 at pressure ratio 3 and flow rate of 13 g/s. Upon increasing rotational speed by 19% up to 250,000 rpm, pressure ratio 4 and air flow rate 15 g/s is also found to be achievable.

**Table 7: Specification of Impeller and Diffuser**

Corrected air flow rate -	$G_{a\text{ cor}} = 13 \text{ g/s};$
Total pressure ratio -	$\pi_c^* = 3.0;$
Impeller outer diameter -	$D_2 = 40 \text{ mm};$
Inlet air temperature -	$T_1^* = 288 \text{ K}^0;$
Inlet air pressure -	$P_1^* = 101.3 \text{ kPa};$
Corrected rotational speed	$n_{\text{cor}} = 210000 \text{ rpm}.$

**Table 1**

G	$\pi_c^*$	Efficiency
13.5	3.15	0.69
14.4	3.06	0.68
15.2	2.84	0.647
15.5	2.715	0.618

**Table 8**

<b>Air Flow Rate (corrected)</b>	Ga cor = 13 g/s	15 g/s
<b>Total Pressure Ratio</b>	$\pi^*c = 3.0$	4.0
<b>Impeller</b>	RPM=210,000 rpm	RPM=250,000 rpm
outer diameter	D2=40 mm	
inner diameter	D1=14 mm	
number of blades	Z=8	
blade height	b1=3 mm (inner), b2=1mm (outer)	
blade angle	$\beta_{1b}=35$ deg (inner), $\beta_{2b}=76$ deg (outer)	
inlet Mach no.	M1=0.296 (abs) , Mw1= 0.566 (relative)	0.356 (abs), 0.669 (relative)
inlet flow angle	$\beta_1=30.85$ deg (relative)	31.09 deg (relative)
<b>Diffuser</b>		
outer diameter	D4=60 mm	
inner diameter	D3=45 mm	
number of blades	Z=10	
blade height	b4=b3=1 mm	
blade angle	$\alpha_{3b}=12$ deg (inner), $\alpha_{4b}=24$ deg (outer)	
Mach no.	M3=0.165 (inner), M4=0.104 (outer)	0.154 (inner), 0.097 (outer)
flow angle	$\alpha_3=12$ deg (inner), $\alpha_4=24$ deg (outer)	10.4 deg (inner), 19.1deg (outer)

Mach number contours at different blade height are shown in Figure 41 to Figure 44, whence a large separation zone is apparently seen at the pressure side of radial diffuser vane.

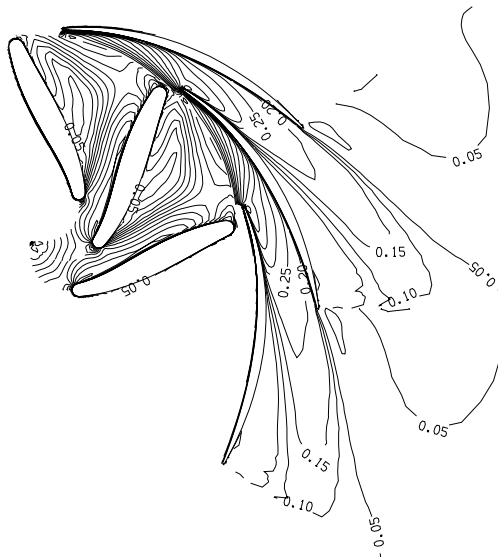


**Figure 41: Mach Number Contours Close to Hub Section.**

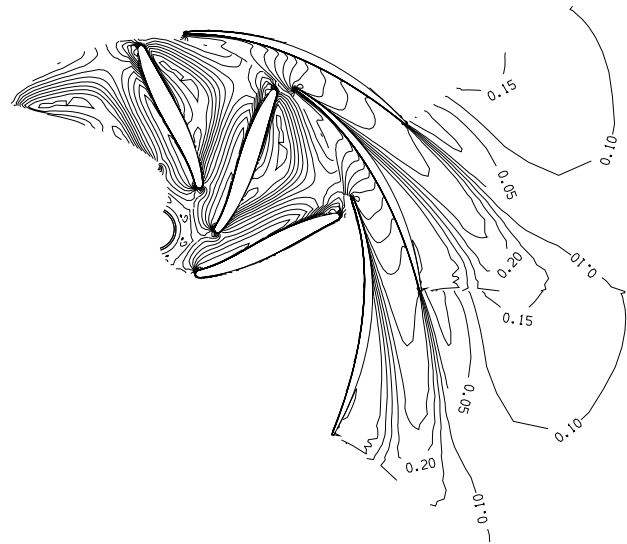


**Figure 42: Mach Number Contours at Mean Section.**



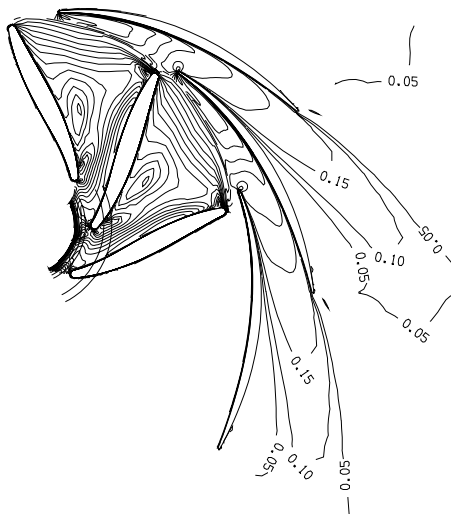


Figure 43: Mach Number Contours Close to Tip Sect.

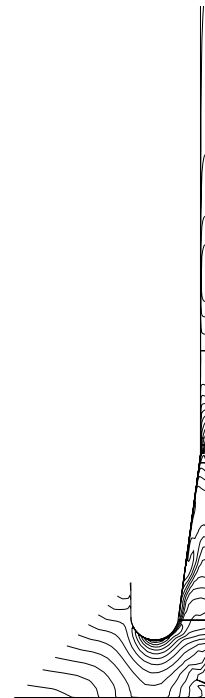


Figure 44: Mach Number Contours in Mean Meridional Section.

For radial turbine, inlet total pressure was calculated by the design pressure ratio 3, but subtracting from it the losses due to compressor inlet and combustor of 1.5% and 10%, respectively. The inlet air flow rate is 13.1 g/s at atmospheric 101.3 kPa, to which standard hydrocarbon fuel is added to result in the turbine inlet gas flow rate 13.4 g/s. The results obtained from numerical simulation are listed below. Rotor tip clearance effects were not considered. The initial type of nozzle and rotor were redesigned into another, for better control of flow separation to decrease the total loss coefficient, wherein laminar flow separation due to low Re number was responsible. This redesign from type 1 to type 2 improved the turbine efficiency by +3%, e.g. total-to-static efficiency from 0.683 to 0.710. Figure 45 and Figure 46 compare Mach number contours between type 1 and 2 at the mid blade height. Intensive separation observed in type 1 at the rotor blade suction surface was very much improved, which are also reflected in Figure 49 showing Mach number distributions around rotor blade surface.

Table 9

rotational speed	210,000 rpm
pressure ratio	2.66
mass-flow rate	13.4 g/sec
efficiency	0.756 (total-to-total), 0.68(total-to-static)
inlet total temperature	1223K
speed ratio	$U/C_0 \sim 0.59$
specific heat ratio	1.35
gas constant	287.4 J/kg/K
<b>Nozzle</b>	
outer diameter	51.3 mm
inner diameter	44 mm
number of blades	18 (Nozzle 1)
blade height	2 mm
exit flow angle	11.88 deg
<b>Rotor</b>	
outer diameter	40 mm
inner diameter	24 mm
number of blades	17 (Rotor 1), 22 (Rotor 2)
blade height	2 mm
inlet flow angle	69.1 deg (relative)
exit flow angle	44.5 deg (relative), 90.6 deg (abs)

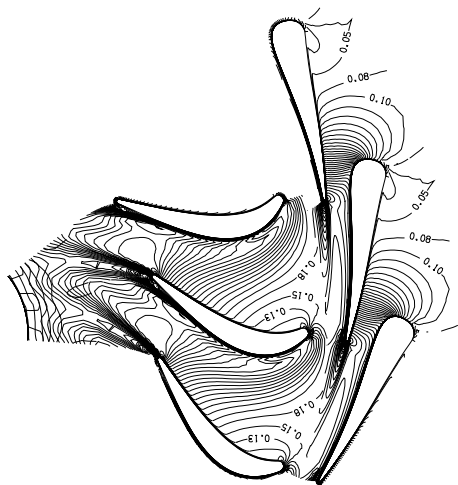


Figure 45: Mach Number Contours at Mean Section of Flow Passage (Version: Nozzle1+Rotor1).

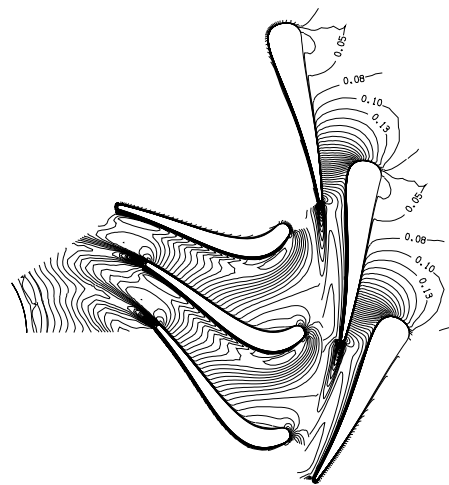


Figure 46: Mach Number Contours at Mean Section of Flow Passage (Version: Nozzle2+Rotor2).

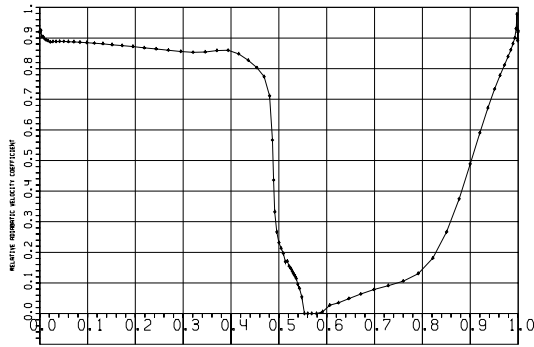


Figure 47: Isoentropic Laval Number Distribution along the Profile Arc Length of Nozzle1 (mean section).

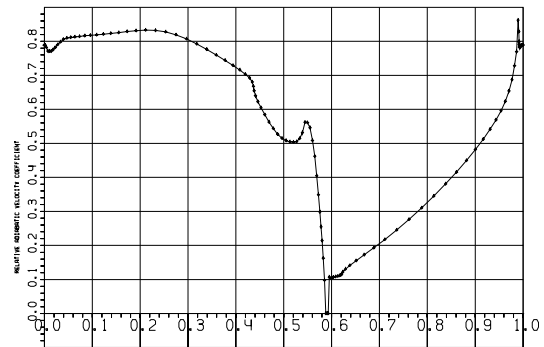


Figure 48: Isoentropic Laval Number Distribution along the Profile Arc Length of Rotor1 (mean section).

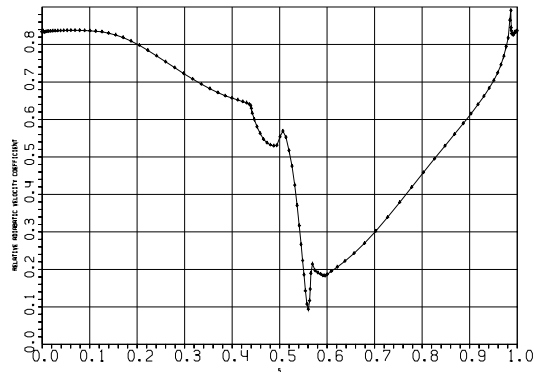


Figure 49: Isoentropic Laval Number Distribution along the Profile Arc Length of Rotor2 (mean section).

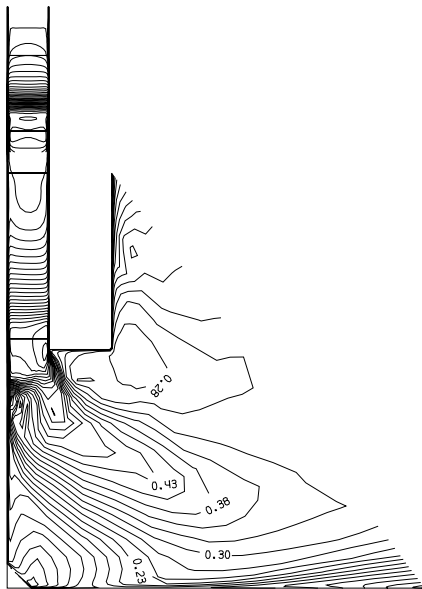


Figure 50: Mach Number Contours in Mean Meridional Section.

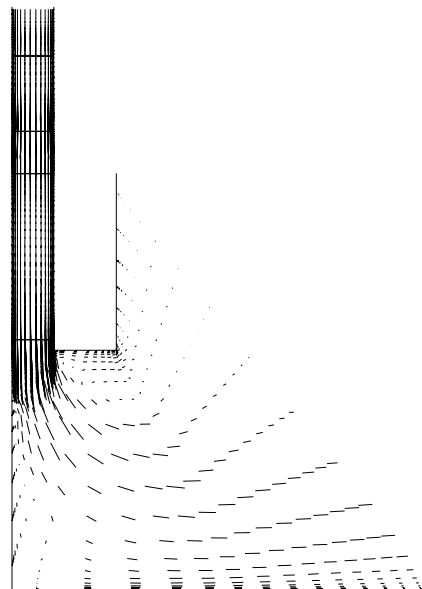


Figure 51: Velocity Vector Field in Mean Meridional Section.

### 4.3 Experiments

#### 4.3.1 Facility and Operations [2]

Test run for gas turbines is often started by either using an electric motor attached to the drive shaft or blowing jets into compressor or turbine rotors, which causes sometimes difficulty, in particular, when the mass flow rate is not well matched between compressor and turbine. Two methods for starting the rig operation presently are schematically shown in the figures below. Both utilize air source installation, but starting motor is not necessary. Air-assist is fit for measurements of the mass flow rates at matched condition of compressor and turbine, enabling to estimate component efficiency  $\eta_{all} = \eta_c \eta_T \eta_m$ , while air pressure-assist is simpler in valve handling to find the latter at various pressure ratio.

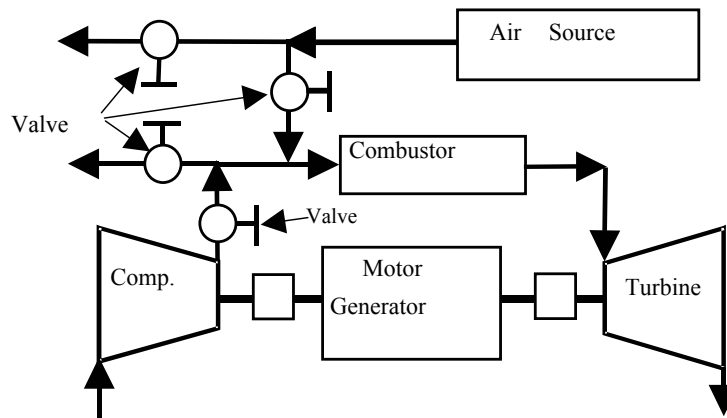


Figure 52: A Facility used as both an Air-Assist Starter and a Test Rig to Measure the Total Efficiencies.

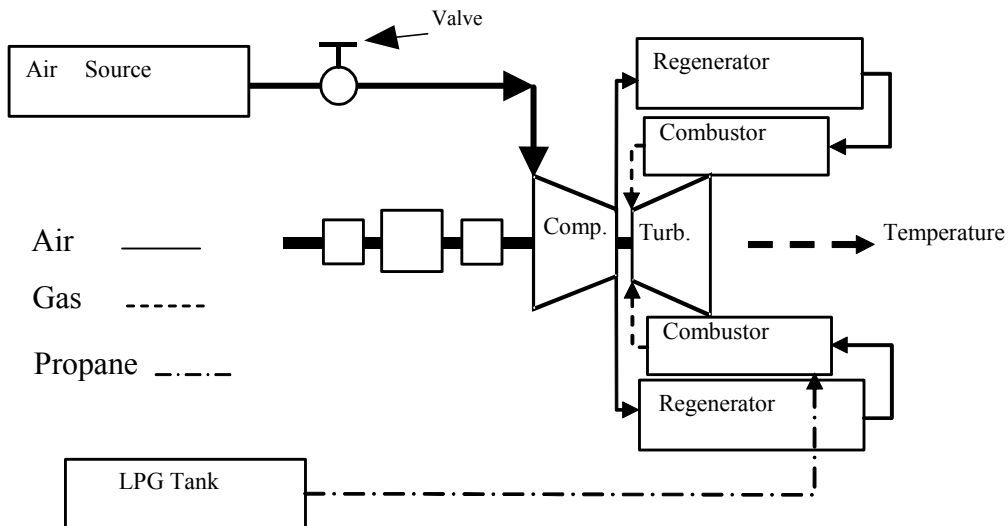


Figure 53: Test Facility of Air Pressure Assist Method.

#### 4.3.2 Preliminary Results [2]

An example amongst preliminary tests results is shown in top of Figure 54, wherein air pressure-assist method was employed to observe that rotational speed very much depends upon assist pressure, for instance,

140,000rpm at 45 kPa. Hot run test results are also shown in bottom of Figure 54. It can be seen exhaust gas temperature was raised to 1,000C and rotational speed was increased proportionally to assist pressure, but little dependent upon the rise in exhaust gas temperature.

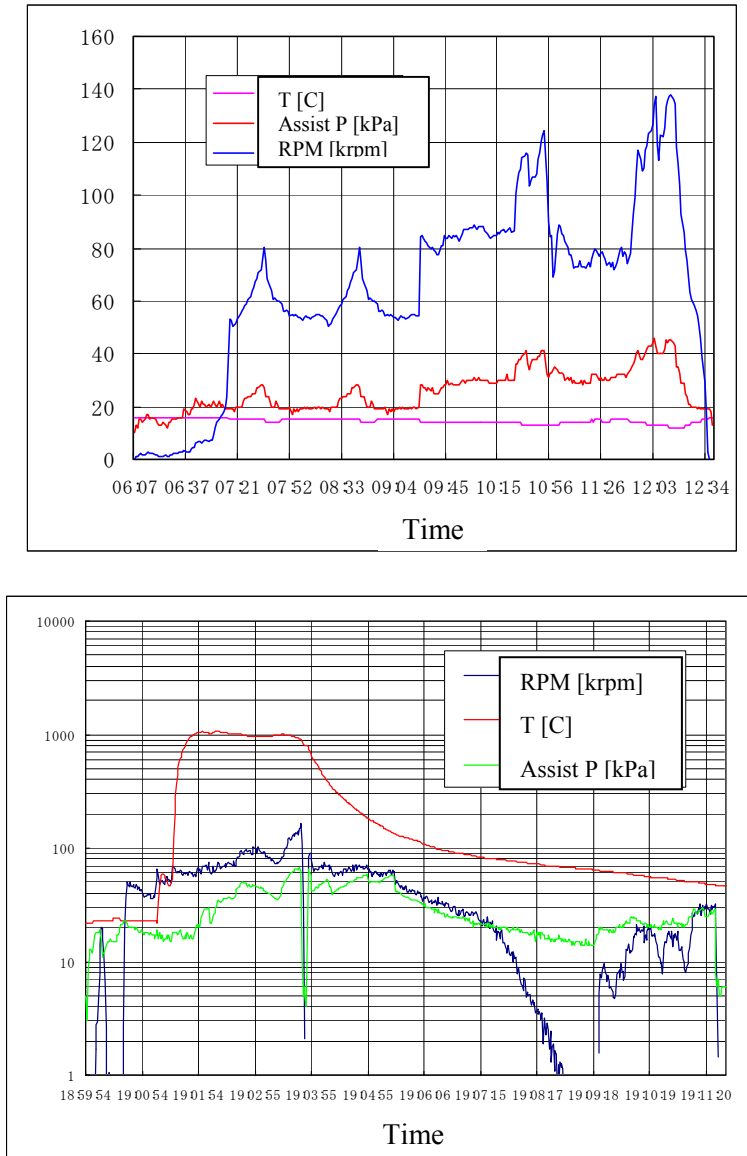


Figure 54: Air Assist Test without Combustion.

## 5. FINGER-TOP FEASIBILITY

### 5.1 Design Particulars

#### 5.1.1 System Integration [2, 17]

Finger-top designing can be considered in several fashions. Meanwhile, a design similar to that for Palm-top is presented in the following, but another configuration installing single can type combustor, for instance, is an alternative choice, if the combustor has to be either isolated or conveniently integrated with micro

recuperator for the purpose of better heat management. In Figure 56, Finger-top is arranged into a single bolt and nut structure to achieve the easiest assembly of as least as possible parts. The scrolls can be also disassembled to easily adapt to any geometry changes in turbine and compressor, wherein a particular care was taken for preventing leakage by means of precise composition integrity with well polished interface parts. Bearings employ the herringbone type with a flange attached for installation and the ultra micro tilting pad type (shaft diameter of 3mm), together with thrust bearings at the side. In order to prevent excessive thrust, the degree of reaction for turbine and compressor has to be appropriately set in the aerodynamic design process. A center shaft serves as the rotor for the motor-generator, leaving a sufficient space around the periphery for the stator (details not drawn here).

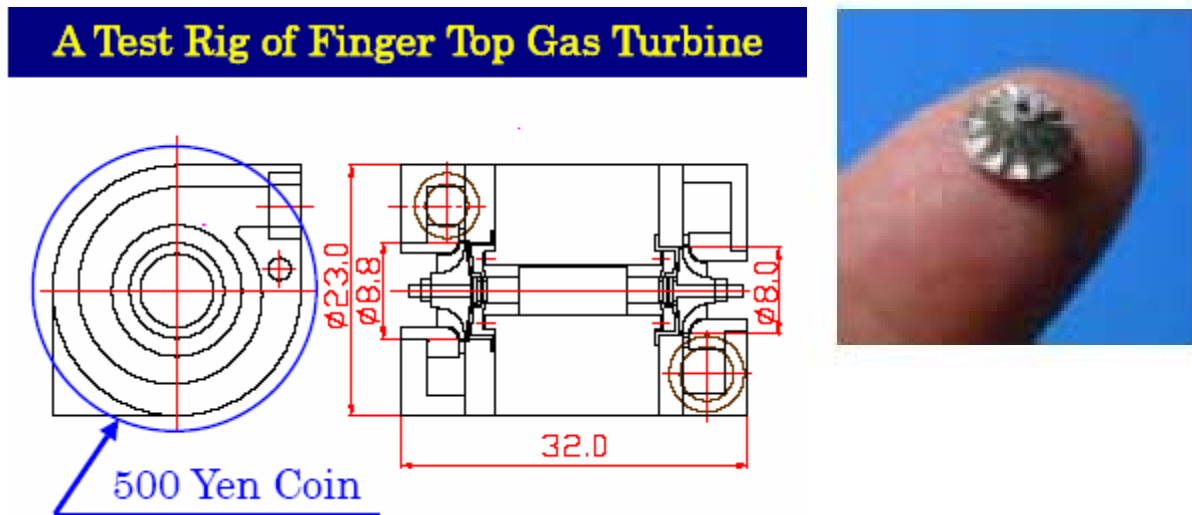


Figure 55: Turbine Rotor 8mm dia.



Figure 56: Finger-Top Turbine Rotor and Centre Shaft.

**Lessons:**

/Technology for rotor dynamics and bearings at high rotational speed is urgently necessary, relating to subjects like 1) stabilization in shaft vibration, 2) load capacity, contacts during start and stop, as well as endurance, of bearings.

/CVD versus Machining: Rotor diameter of 8mm yields blade pitch at the tip of 2.4mm for 10 number of blades, for example, so that blade thickness becomes order of 0.1mm. Chemical Vapour Deposition (CVD) and etching are likely applied for that size, but it is also close to the extreme of machining manufacture. Figure 57 compares 2D profiles by employing CVD and 3D profiles by 5-axis NC machining process, whence the latter is also satisfactory with regard to surface smoothness and tolerance. In particular, capability of 3D shaping looks very attractive from aerodynamic point of view, so that manufacture technology is explored for requisite materials and mass production to satisfy cost requirement.

/Heat transfer between hot turbine and cold compressor causes substantial decrease in thermal efficiency. According to the analysis model in Figure 58, heat transfer between the compressor and turbine rotors was estimated to decompose into the following ratio at each heat path: through the space ring, 58%, radiant heat, 28%, and through air and the dividing plate, 15%. Therefore, the space ring material was changed from stainless steel to ceramic, and to insert a reflecting plate at the center of the divide plate.



**Figure 57: 8mm Turbine Wheels.**

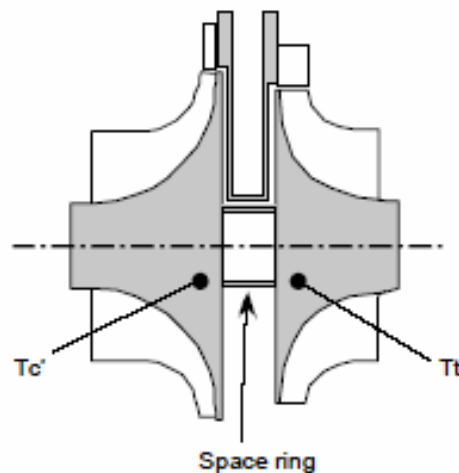


**Figure 58: A Heat Transfer Analysis Model.**

### 5.1.2 Gas Bearings and Rotor Dynamics [24-29]

A proposition herein is the evaluation methodology of dynamic characteristics of small size rotor supported by gas bearings in general. In order to operate small size MGT systems, the information on the natural frequencies corresponding to lateral, conical, the first bending mode and the onset whirl rotational speed are indispensable. In the following, the procedure based on the measured rotational speed and vibrations of the rotor will be introduced.



*Evaluation of Bearing Stiffness, Damping Coefficients and 1<sup>st</sup> Bending Natural Frequency*

Figure 59 shows the typical rotor supported with two radial gas bearings fixed to the housing. If the stiffness of the bearing is small enough compared with the bending stiffness of the rotor, the rotor may be modelled as rigid. Figure 60 shows the mathematical model for the rigid rotor supported by linear springs and dashpots.

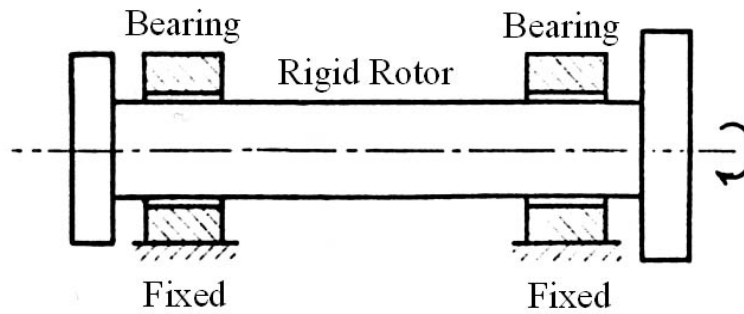


**Figure 59: Bearing Supported Rigid Rotor.**

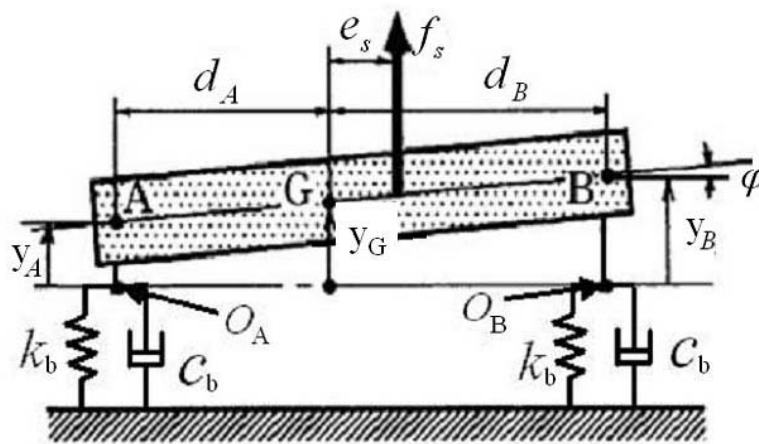


**Figure 60: Mathematical Model for Bearing Supported Rigid Rotor.**

By increasing the rotor speed of our test rotor, vibration data as shown in Figure 61 are obtained.

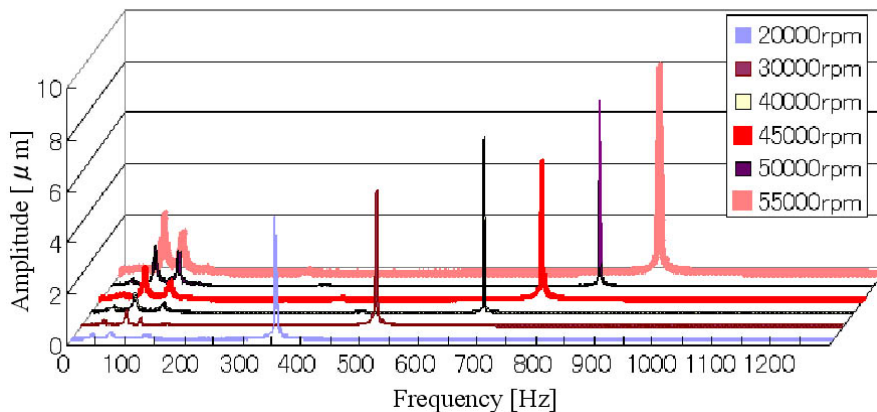


**Figure 61: Frequency Spectra of the Rotor Vibrational Amplitude.**

From Figure 61, the corresponding natural frequencies are identified for the first and the second rigid mode as 75Hz and 115Hz. By employing complex eigenvalue analysis, bearing stiffness and damping coefficients are determined as  $k_b = 420000$  [N/m] and  $c_b = 538$ [N×s/m].

Actual small size MGT has complex geometries and flexibility, therefore, FEM for analyzing natural frequencies are usually employed. In Figure 62, analyzed results for 1<sup>st</sup> bending natural frequencies taking account of bearing stiffness and damping are shown as a function of rotational speed.

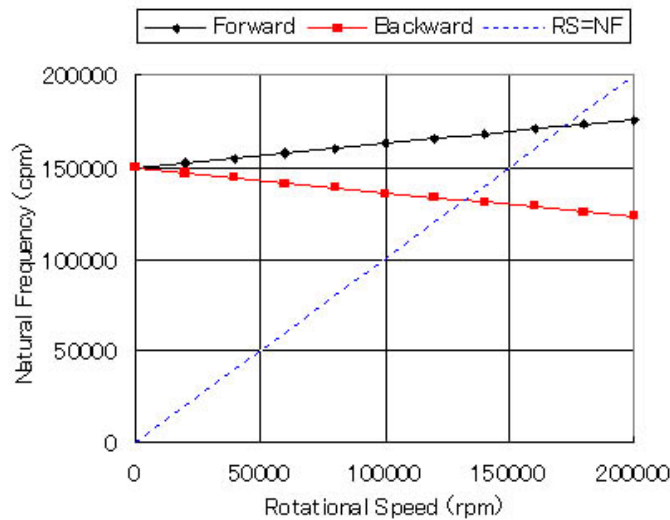


Figure 62: 1<sup>st</sup> Bending Natural Frequency of Bearing Supported Flexible Rotor.

#### Evaluation of Onset Whirl Speed

From the viewpoint of safety operation, it is necessary to predict onset whirl speed from the monitored data operated under whirl speed. Design and manufacture were made for a simple test rig for measuring dynamic stiffness ( $K_{xx}$ ,  $K_{xy}$ ,  $K_{yx}$ ,  $K_{yy}$ ) of the bearing as shown in Figure 63 to succeed in obtaining necessary data which are summarized in Figure 64. Then, based on these data, calculation for predicting onset whirl velocity was carried out to obtain 72000rpm in this case, which seems reasonable.

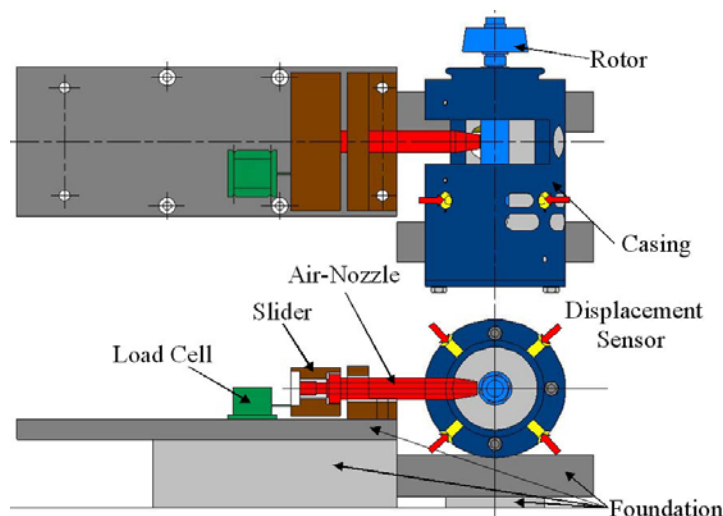


Figure 63: Test Rig for Measuring Dynamic Stiffness.

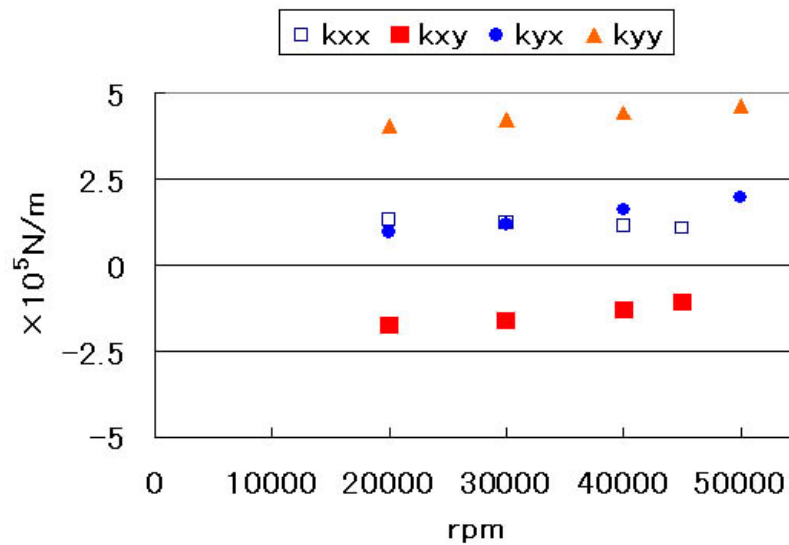


Figure 64: Dynamic Stiffness Coefficients.

### 5.1.3 Heat Exchanger [2, 30]

For Finger-top size, a micro-channel MEMS recuperator will be appropriate. As shown in Figure 65, simple square channel configuration with  $Dh = 0.5\text{mm}$ ,  $\delta_w = 0.1\text{mm}$  and  $\delta_{wb} = 0.2\text{mm}$ , yielding 60% porosity, was assumed for an examination. The effect of axial heat conduction in the wall has to be taken into account, so that silicon was chosen as a representative MEMS material. Under the cycle specification noted in Figure 65 and at the gas flow rate of 0.15 g/s, the recuperator volume was designed to be 3 cm<sup>3</sup>, giving the ratio between volume and mass flow rate to be 0.020 m<sup>3</sup>/(kg/s), with target effectiveness around 0.8, the same as that in the offset strip fin type for Palm-top. Thermal efficiency will be improved from 5% to 10%, by adopting a recuperator with this level of effectiveness. Figure 66 show the dependence of effectiveness, pressure loss and thermal efficiency upon the length  $L$ , with varying  $Dh$ . Fully developed laminar flow ( $Nu = 3.6$ ,  $Cf = 14.2/Re$ ) was assumed inside a channel, so that the smaller  $Dh$  gives inversely the larger heat transfer rate, which yields higher effectiveness, while heat conduction in the wall deteriorates it as  $L$  gets smaller. (Figure 66.a) The smaller  $Dh$ , however, brings about rapid increase of pressure loss (Figure 66.b), so that thermal efficiency reveals a peak amongst the curves with varying  $Dh$  and  $L$  parameters, that is, presently, at about  $Dh = 0.5\text{mm}$  and  $L = 40\text{mm}$ . (Figure 66.c). In order to realize the optimum path length  $L$  within a limited volume installing the rotor of 8mm dia. in Finger-top, an appropriate suggestion may be to employ multi-, for instance, three-path configuration shown in Figure 67.

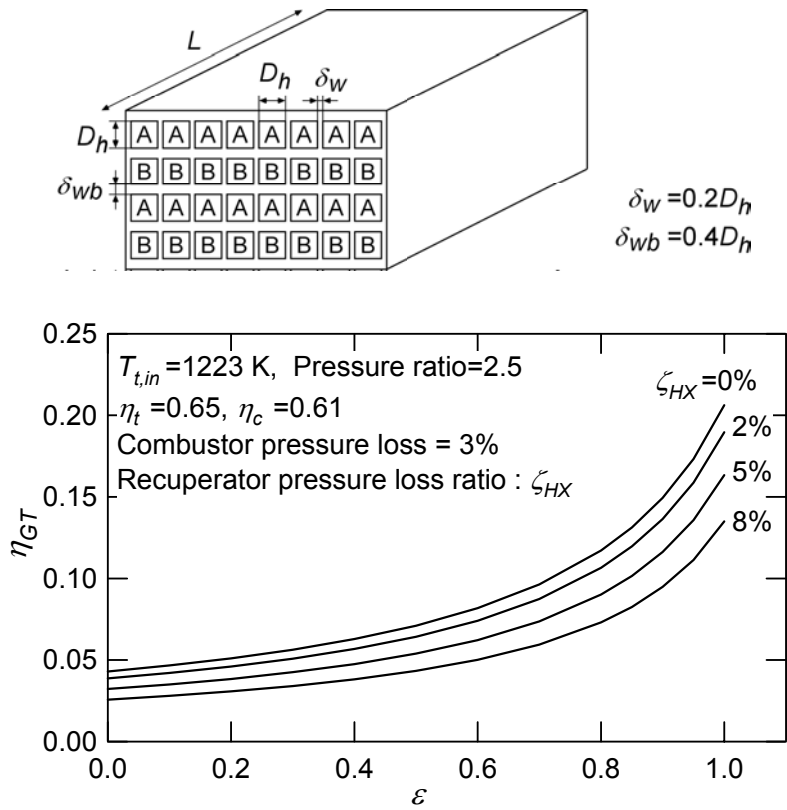


Figure 65

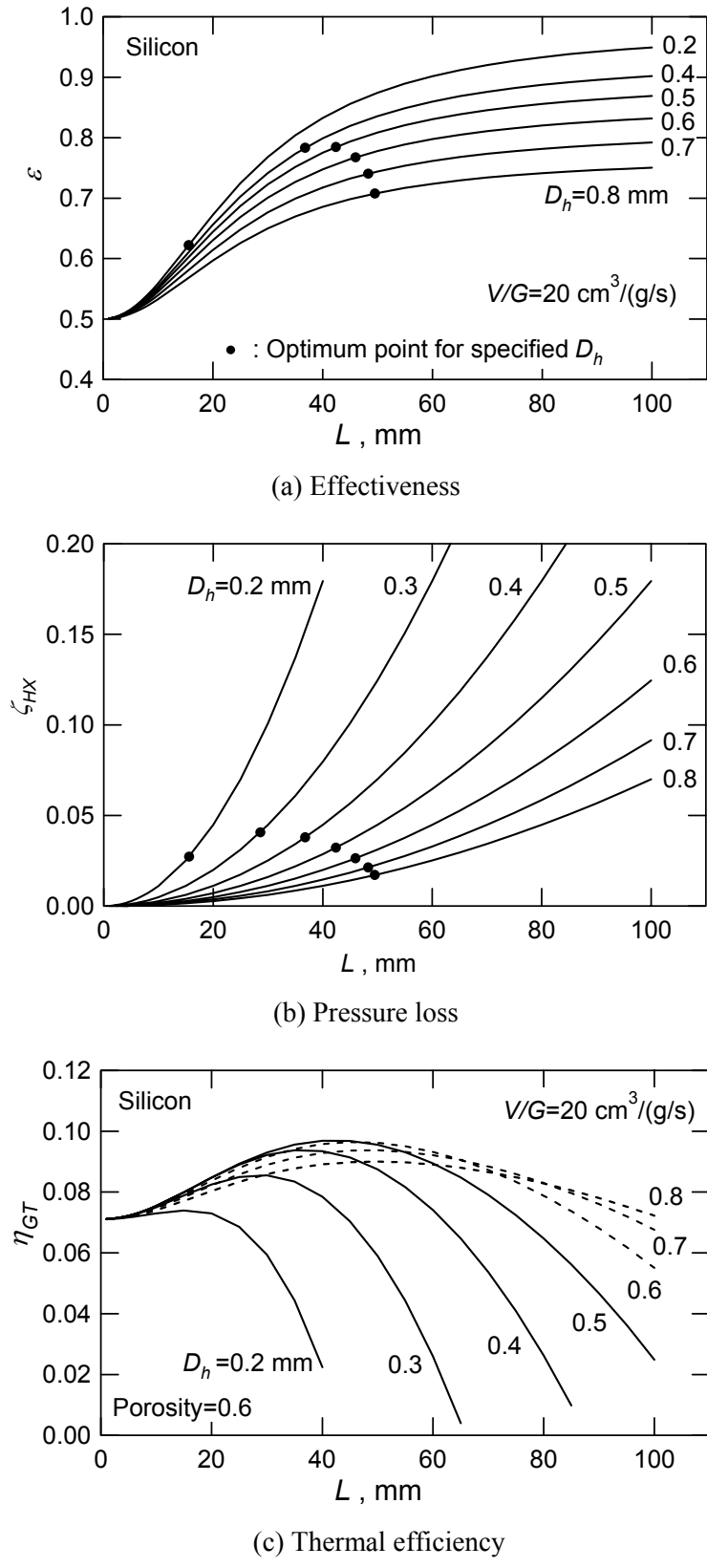


Figure 66

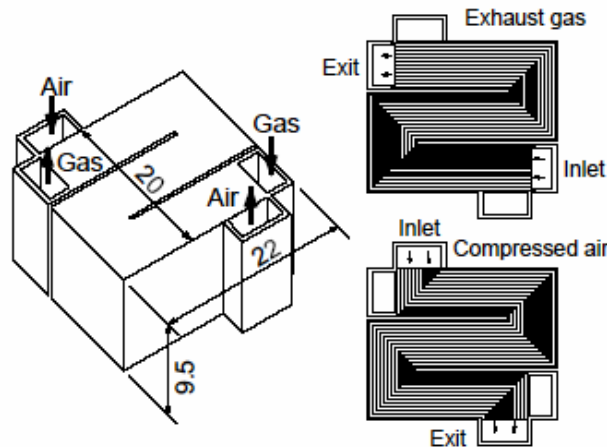
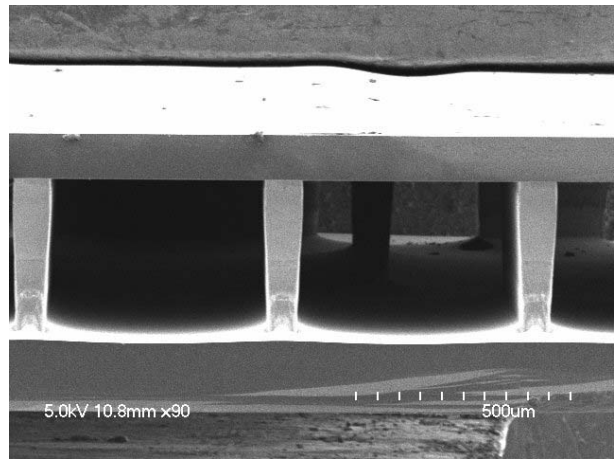


Figure 67: Micro Recuperator Example for 15W turbine (exhaust gas: 8 layers, air: 7 layers,  $\epsilon=0.8$ ).

**Lessons:**

/Difficulties associated with MEMS recuperator are concerning, first, the mechanical strength of silicon material against high temperature, and second, fusion bond fabrication technique. Under the present Finger-top specification, the turbine exhaust temperature exceeds 1,000K, while the effectiveness of 0.8 yields the max. channel wall temperature of 980K, both not recommendable for use of silicon. The figure on the right shows an attempt of fusion bonding 100 $\mu\text{m}$  wafer upon ICP (Inductive Coupled Plasma) DRIE pattern of 400 $\mu\text{m}$  square open channel with 100 $\mu\text{m}$  fin walls.



/Non-MEMS compact recuperator, that is, a unit separately installed from the core gas turbine, may be worth explored for various practical applications. Figure 68 shows the results of micro channel optimization over a range of V/G ratio. Materials are also compared between stainless steel and silicon, since the abscissa V/G needs drastic increase to raise effectiveness beyond 0.8, so that the corresponding channel size becomes of the order 0.4mm, applicable for metal fabrication. Stainless steel behaves better because of smaller heat conductivity.

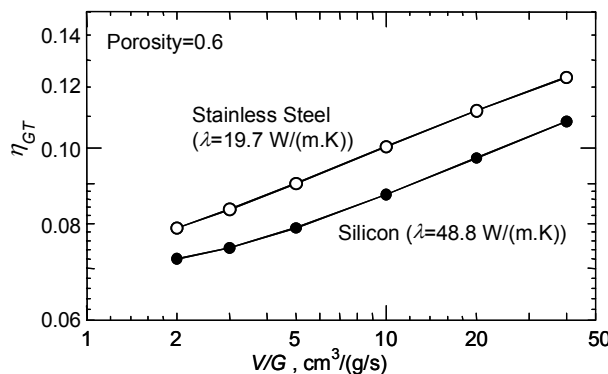


Figure 68: Optimization of Micro Channel with Respect to V/G. (Stainless Steel vs. Silicon).

### 5.1.4 Electric Motor-Generator [2]

Electrostatic induction type becomes beneficial for its simple structure over magnetic type as it gets smaller in size to such an extent that electric field can be extremely intensified. Examining each sectional view at the same diameter in Figure 69 or Figure 70, the critical size is dominantly determined by either the effective core rod length (the hatched part in Figure 69) or the air gap, respectively, for magnetic and electrostatic induction types.

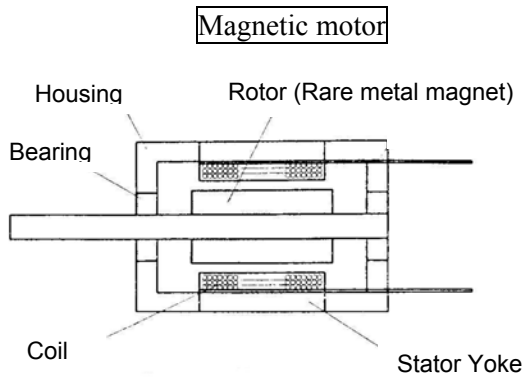


Figure 69: Cross-Section of Magnetic Motor.

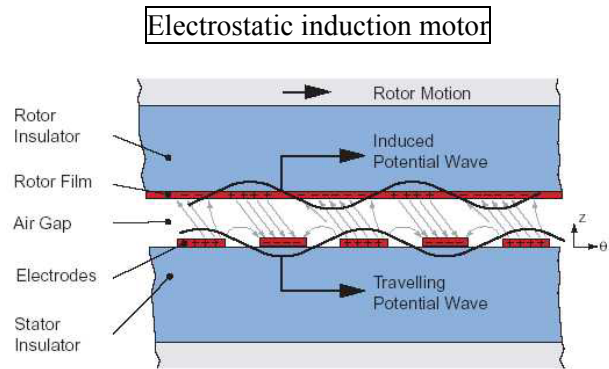


Figure 70: Cross-Section of Electrostatic Induction Motor.

The power output  $P$  may be obtained by the following formula:

$$P = \omega T^{10)}$$

$P$ : Power[W]  
 $\omega$ : Frequency[rad / sec]  
 $T$ : Torque[Nm]

$$T = \frac{\pi}{2} k_R k_w ac \bar{B}_g D^2 \ell_i \cos \phi$$

$k_R$ : Form factor  
 $k_w$ : Winding factor  
 $ac$ : Electric loading[Number of turns / m]  
 $\bar{B}_g$ : Magnetic flux density[T]  
 $D$ : Rotor diameter[m]  
 $\ell_i$ : Effective wire length[m]  
 $\cos \phi$ : Phase angle

$$P = \omega T^9)$$

$$T = \frac{\pi m \epsilon_0 V^2}{4 g_m (1 + \frac{\epsilon_b g_m}{\epsilon_0 \Delta})} (r_{mo}^2 - r_{mi}^2)$$

$m$ : Phases  
 $\epsilon_0, \epsilon_b$ : Permittivity[F / m]  
 $V$ : Voltage[V]  
 $g_m, \Delta$ : Motor gap & thickness[m]  
 $r_{mo}, r_{mi}$ : Outer & inner radii[m]

$$m \omega = 2\pi f$$

It may be postulated that an appropriate motor-generator for MIT Power-MEMS turbine, for instance, needs the design parameters, geometry and property coefficients as listed in Table 10, whence the formula above can provide the relation between length and power.



Table 10: Design Parameters

Electrostatic induction motor

【Design parameters】

Parameters	Symbol [Unit]	Value
Voltage	V[V]	400
Rotational speed	N[ $\times 10^4$ rpm]	24, 120, 240

【Geometry】

Parameters	Symbol [Unit]	Value
Outer radii	$r_{mo}$ [mm]	2
Inner radii	$r_{mi}$ [mm]	1
Dielectric thickness	$\Delta$ [ $\mu$ m]	10
Motor gap	$g_m$ [ $\mu$ m]	0.37, 3.7, 37

【Permittivity】

Parameters	Symbol [Unit]	Value
Permittivity of vacuum	$\epsilon$ [F/m]	$8.85 \times 10^{-12}$
Permittivity of air	$\epsilon_0$ [F/m]	$(1 + 5.36 \times 10^{-4}) * \epsilon = 8.85 \times 10^{-12}$
SiO <sub>2</sub> Relative permittivity (permittivity $\epsilon_b$ )	$\epsilon_b$ [F/m]	$4.0(3.54 \times 10^{-11})$

Magnetic motor

Parameters	Symbol [Unit]	Value
Rotational speed	N[ $\times 10^4$ rpm]	24, 120, 240
Rotor diameter	D[mm]	4
Phases		3
Pole pitch		$\pi D / \text{phases} = 4.19$
Form factor	$K_R$	1.11 (phases 3)
Phase angle	$\cos \phi$	0.9
Magnetic flux density	$B_g$	$2/\pi$
Winding factor	$K_w$	$3/\pi$

The calculation results are thus plotted in Figure 71, which indicates that electrostatic induction will be a better choice if the magnetic core length can not be longer than a max order of  $10^{-5}$  m. Whilst, power obtainable for electrostatic induction will be limited by max about  $10^2$  W at the speed of 2.4 million rpm,

unless air gap is kept precise control beyond the order of  $10^{-6}$  m, that will be a pretty tough dynamic requirement for bearings at such a high speed rotation.

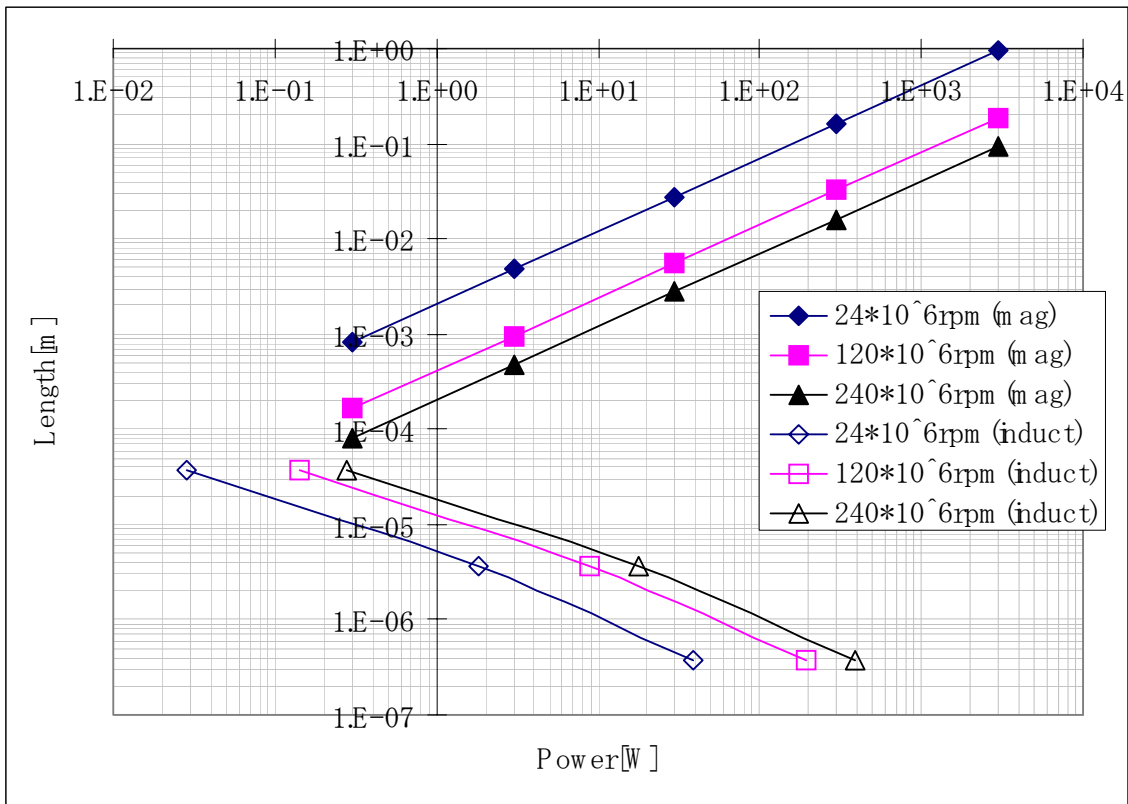


**Figure 71: Relation between Length and Power (Magnetic motor & Electrostatic induction motor).**

Another difficulty is encountered by viscous loss associated with the relative rotation between two discs at very narrow gap. A simple Couette flow assumption, if applied to MIT Power-MEMS turbine rotors the above, leads to viscous work at atmospheric constant viscosity as shown in Figure 72, resulting the work up to 170W at 1.0 million rpm with a gap of  $3 \mu\text{m}$ .

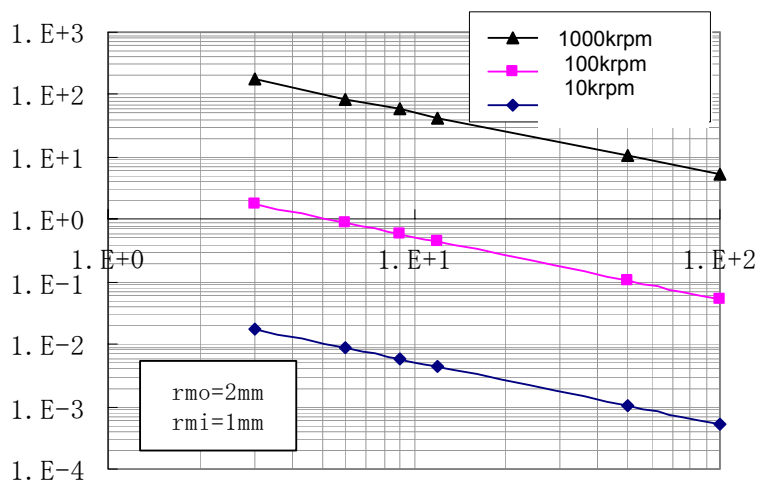


**Figure 72**

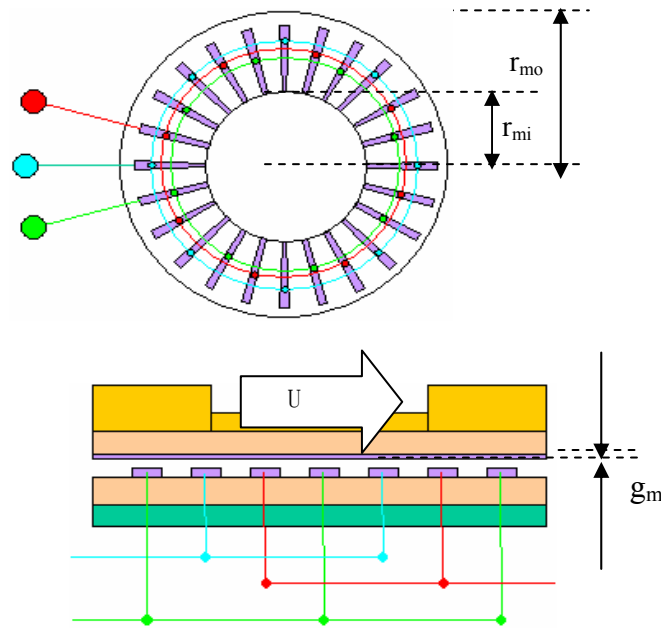


Figure 73

Currently feasible choice is therefore of permanent magnetic type, but its size needs to be in match with Finger-top design. The design target was 8.8mm in dia. and 6.4mm in length, compatible with gas bearing operation at several hundreds krpm. The specification thus determined is listed in Table 11 below.

Table 11: Specification of Motor-Generator

Item	Unit	Spec
Size	mm	outer dia: 8, length: 18.5
Generator type		coreless, 3 phase A.C.
Excitation		permanent magnet, 2 poles
Coil type		3 phase star grids
Bearing		ball
Coils		spec-A $\Phi 0.07 \times 180 \text{turn} \times 3 \text{ coils}$
		spec-B $\Phi 0.1 \times 95 \text{turn} \times 3 \text{ coils}$
Torque coefficient (calculated)		spec-A 3.75 mV-sec/rad
		spec-B 1.98 mV-sec/rad

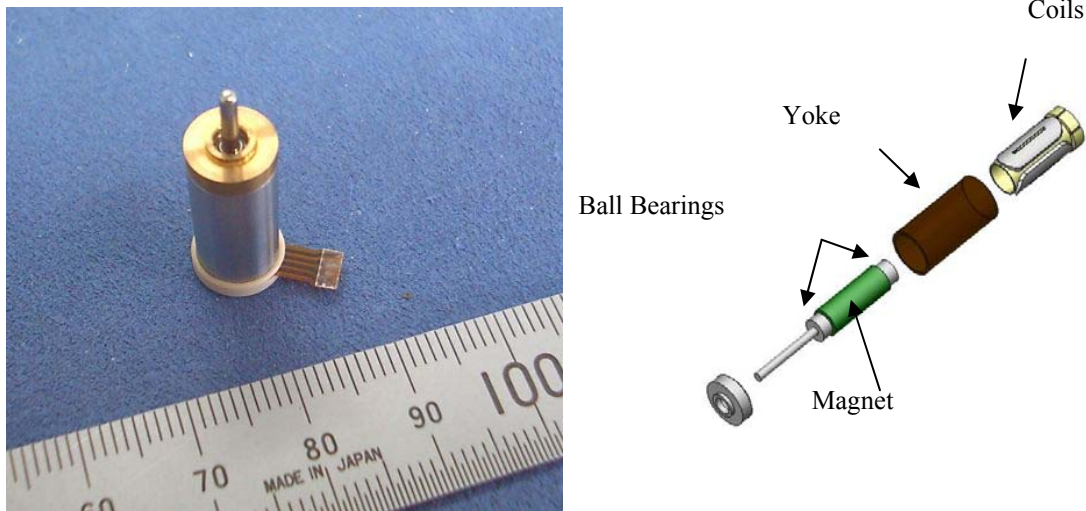


Figure 74: Motor-Generator.

Employing an air turbine drive (max 140krpm, 14W) for machining process, generator performance was tested to yield the results in Figure 75. The power obtained was about 2W for Spec A and 2.5W for Spec. B at 50krpm. At much higher rotation the power loss  $P_c$  due to hysteresis  $P_h$  and eddy currents  $P_e$  inside yoke is likely to be a dominant factor as expressed by the following formula:

$$P_c = P_h + P_e = \sigma_h f B_m^{1.6 \sim 2} + \sigma_e t^2 f^2 B_m^2$$

where,  $P_c$  : yoke loss[W/kg],  $P_h$  : hysteresis[W/kg],  $P_e$  : eddy currents[W/kg],  $f$  : frequency[hz],  $B_m$  : magnetic flux density[Wb/m<sup>2</sup>],  $t$  : yoke thickness[mm],  $\sigma_h, \sigma_e$  : const.

Mitigation has to be found by means of either yoke materials or structural consideration.

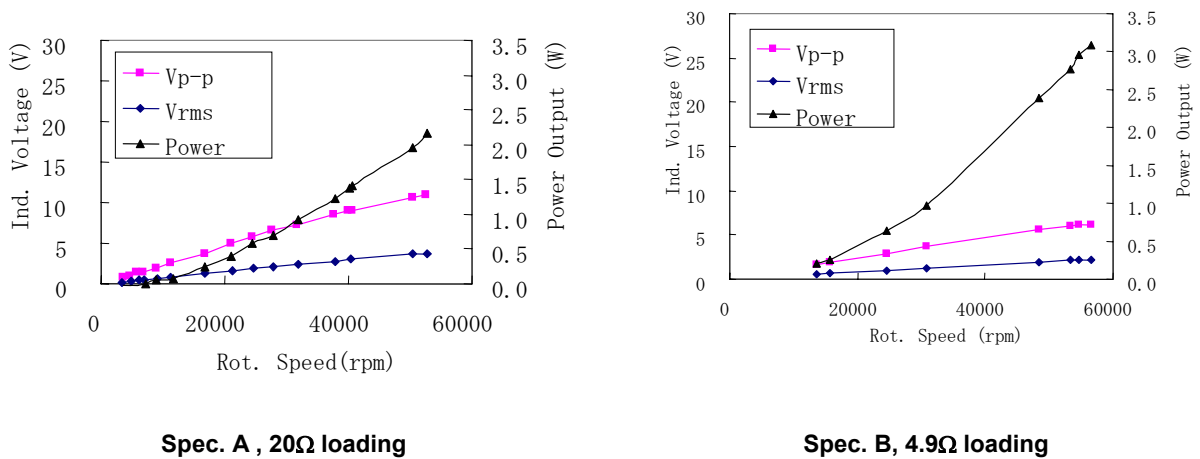


Figure 75: Generator Performance.

**Lessons:**

/The output loss arising from motor-generators, both in electrostatic and magnet types, can be significant at higher rotation, compared with UMG T total output. Associated heat, therefore, has to be managed/ accounted for in the thermodynamic system integration.



Performance predicted is listed as:

Adiabatic efficiency	0.634 (total-to-total), 0.547 (total-to-static)
Pressure ratio	1.98
Mass flow rate	0.75 g/s
Power	74.67 W

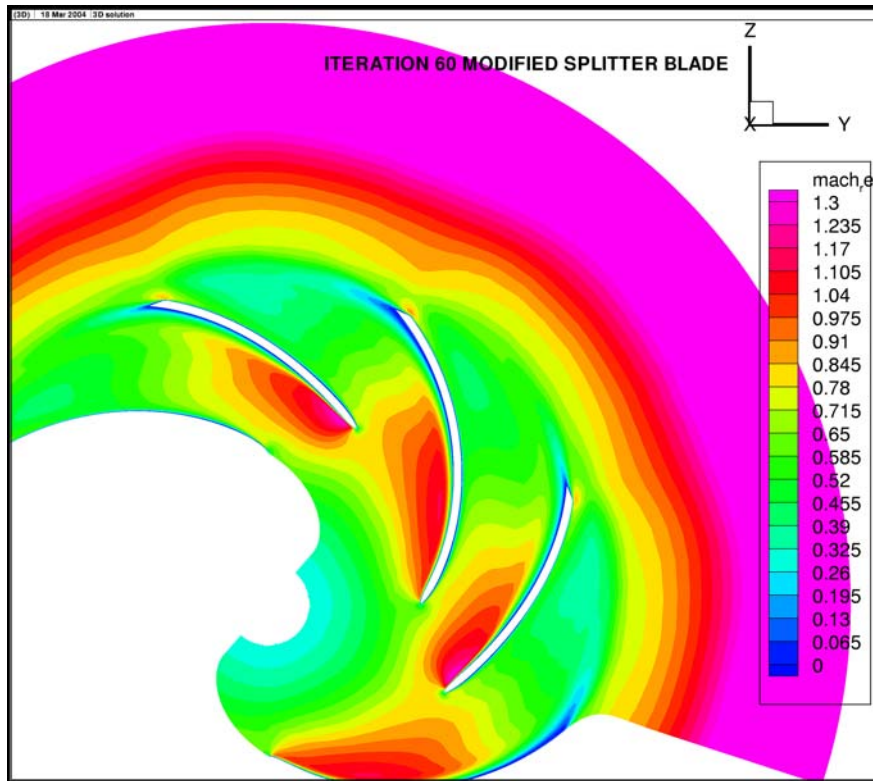


**Figure 77: Isentropic Mach Number Distribution at Mid-Span.**

Figure 78 shows the corresponding pattern of isentropic Mach number at mid-span, and also the latter distributions along the blade surface at hub and shroud in Figure 79. Pitch-averaged velocity distributions in meridional plane is given in Figure 80. While, a prediction of off-design point characteristics is also indicated in Figure 81. Three figures at each point correspond to, from the top to the bottom, adiabatic efficiency (total-to-total), ditto (total-to-static) and power [W].

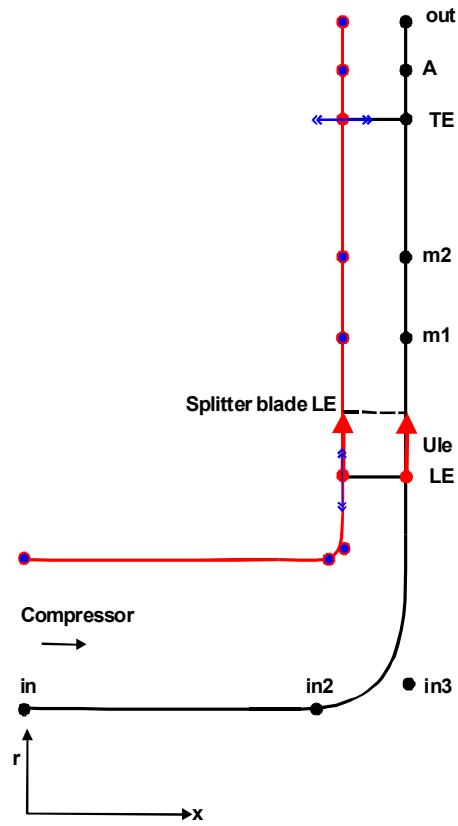


Figure 78: Meridional Configuration (Compressor).

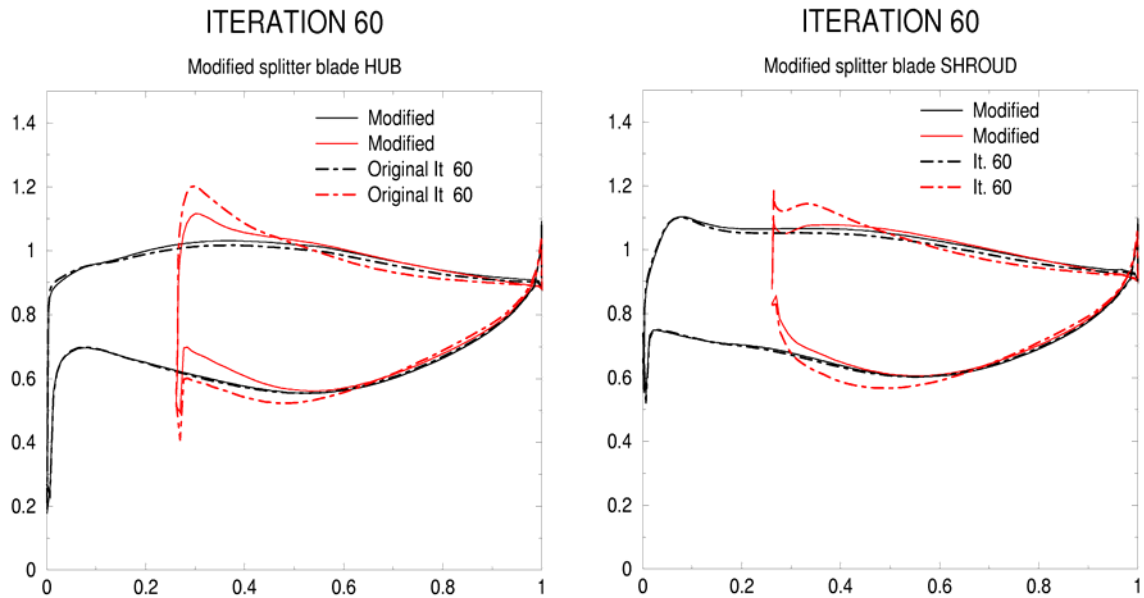


Figure 79: Isentropic Mach Number Distribution Hub (left) Shroud (right).



me 001 | 18 Mar 2004 | 2D solution

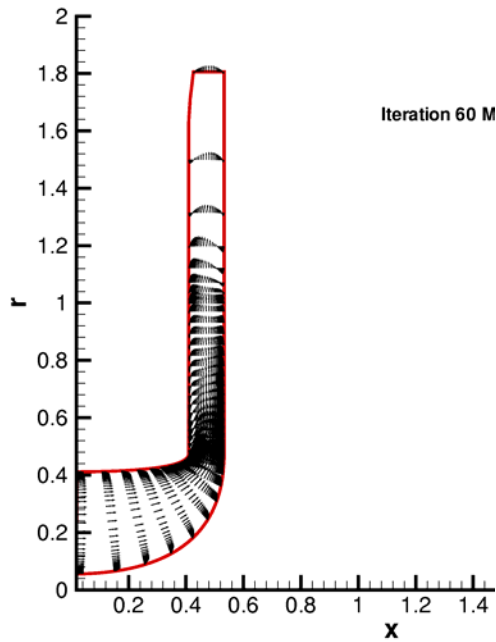


Figure 80: Pitch Averaged Velocity Vectors.

OFF-DESIGN ITERATION 60, Nominal speed

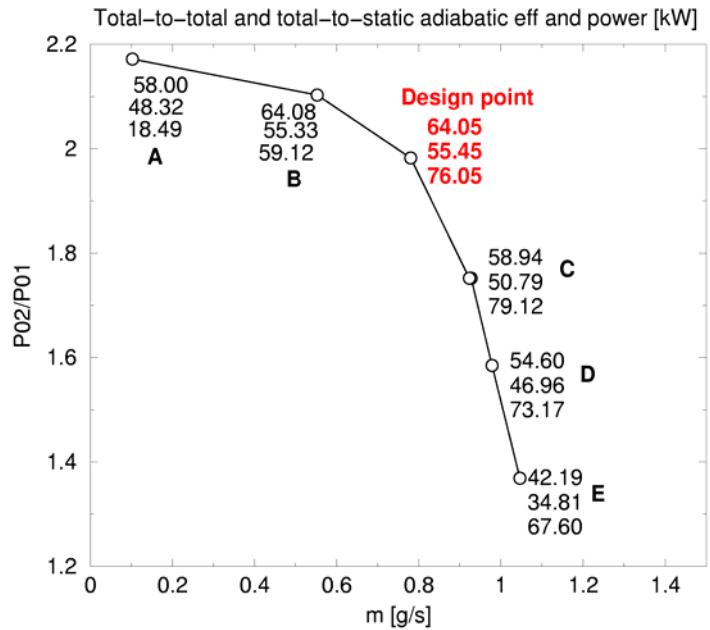


Figure 81: Off-Design Performance at Nominal Speed.

Turbine

The optimization procedure was also applicable to turbine designing. The meridional contour definition is illustrated in Figure 82, where LE radius 4mm and hub wall geometry were fixed. The variables were TE radius, LE width, blade number and blade setting angles. Blade thickness was chosen 0.16mm with elliptic TE, while LE was of sharp cut. Tip clearance was fixed 0.020mm. The optimization resulted in the following specification:

TE radius	4.4mm
LE width (blade height)	0.65mm
Blade number	20
Blade setting angle (at hub)	-11.8 deg at LE, 65.0 deg at TE

The entering gas condition was assumed to be total pressure 288.07 [kPa], total temperature 1223 [K], flow angle (abs) 80.1 deg., uniform across the width.

Performance predicted is listed as:

Adiabatic efficiency	0.927 (total-to-total), 0.906 (total-to-static)
Pressure ratio	1.98
Mass flow rate	0.41 g/s
Power	99.5 W

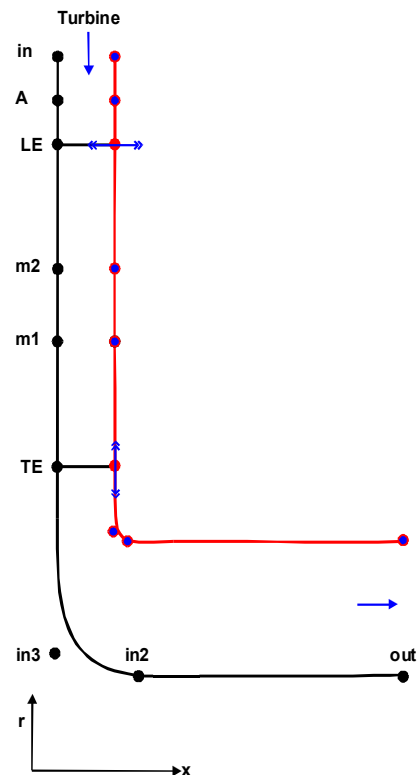


Figure 82: Meridional Contour Definition.

Figure 83 (Right) shows the corresponding pattern of relative isentropic Mach number at mid-span. The latter distributions along the blade surface at hub and shroud is shown in Figure 83 (Left). Pitch-averaged relative velocity distributions at mid-span as well as in meridional plane are given in Figure 84.

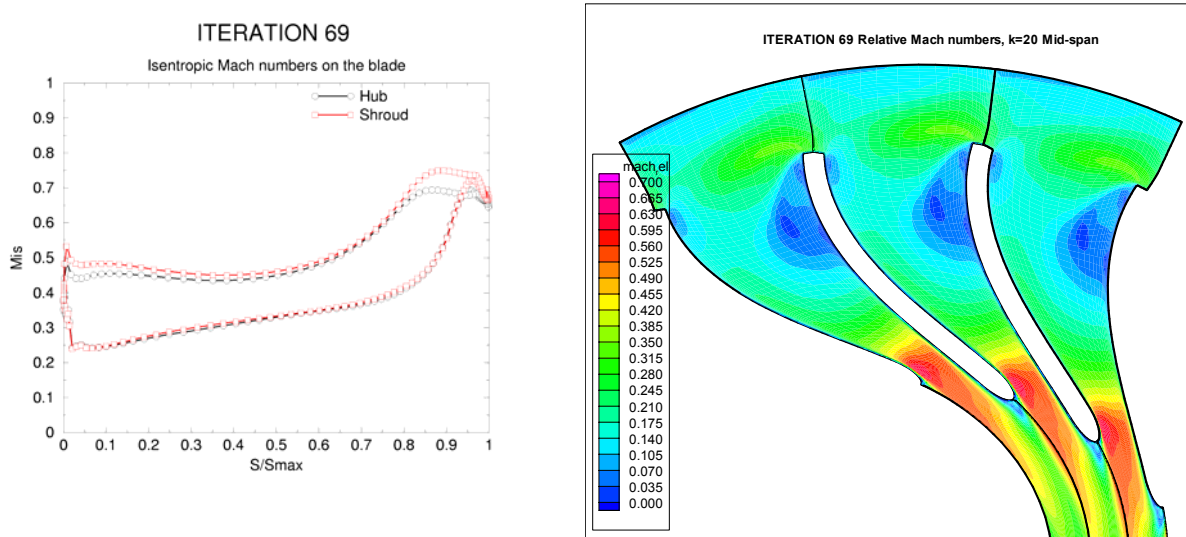


Figure 83: Isentropic Mach Number Distribution on the Blade (Left) Relative Mach Number at Mid-Span (Right).

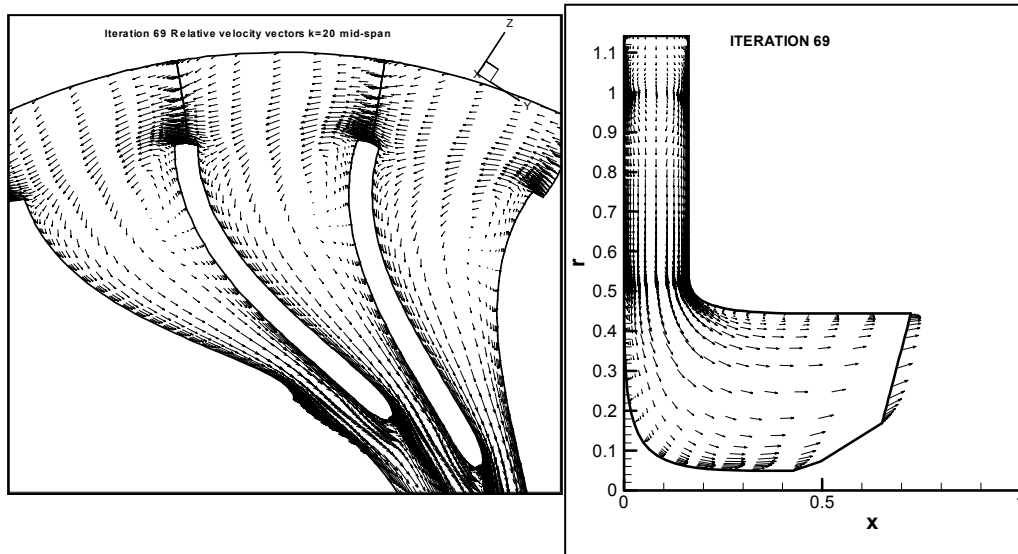


Figure 84: Relative Velocity Vectors Mid-Span (left), Meridional (right).

## 6. CONCLUSION AND SUGGESTIONS

Palm-top regenerative gas turbine cycle engine that achieved the world's smallest and lightest level of 2-3 kW output, dry weight 14.3 kg including generator, 8.5 liters in volume has been prototyped and tested with propane as a main gas fuel. Finger-top gas turbine, installing rotors of 8mm in diameter, that is, 5 times less in scale than Palm-top, was investigated from various designing point of view to conclude that such a tiny engine is feasible to be fabricated by machining. Much more firm engineering knowledge base is necessary for reliability in system integrity and insight of exciting thermo-fluid dynamics in low Re

number, non-adiabatic internal flows, as well as ultra-high rotational lubrication and precise dynamic balance.

Just like in macro application, miniature gas turbines are believed to take an advantage of system composition and working at high temperature level in thermodynamic cycle in realizing significant potential of hybrid usage with other power conversion devices such as fuel cells. That direction of exploration will be certainly needed further, the key technology for a success being the well thought total heat management.

## **ACKNOWLEDGEMENTS**

This work was supported by NEDO International Joint Research Project on Energy and Environment, entitled “Practicing research of button sized gas generators” in FY2001 and “Leading R&D to practice UMG” in FY2002-2003.

## **REFERENCES**

- [1] Practicing research of button sized gas generators, NEDO International collaboration, Report No. 51101591, 2001.
- [2] Leading R&D to practice Ultra Micro Gas Turbines, NEDO International collaboration, Report 2002.
- [3] “Turbines on a dime”, Oct. 1997 by ASME.
- [4] MEMS Transition into DOD Systems, DARPA PI Meeting, 13 January 2000.
- [5] W.C. Tang, Overview of Micro Power Generation Research in United States, Tsukuba, Japan Nov. 12-13, 2002.
- [6] A.H. Epstein et al, “Micro-Heat Engines, Gas Turbines, and Rocket Engines”, 28<sup>th</sup> AIAA Fluid Dynamics Conference, June 1997.
- [7] S. Tanaka et al, “Design and Fabrication Challenges for Micromachined Gas Turbine Generators”, DD-014, ISROMAC-9, 2002.
- [8] S. Tanaka, M. Esashi, Micro-Power Generation Research at Tohoku University, Tsukuba, Japan Nov. 12-13, 2002.
- [9] K. Isomura et al, “Feasibility Study of a Gas Turbine at Micro Scale”, ASME paper 2001-GT-101, 2001.
- [10] K. Isomura, et al., Component Development of Micromachined Gas Turbine Generators, Tsukuba, Japan Nov. 12-13, 2002.
- [11] Kousuke Isomura, Shuji Tanaka et al, “Design Study of a Micromachined Gas Turbine with 3-Dimensional Impeller”, The 9th of International Symposium on Transport Phenomena and Dynamics of Rotating Machinery Honolulu, Hawaii, February 10-14, 2002.
- [12] Robert J. Nowak, DARPA’s Advanced Energy Technologies, DARPATECH 2000.
- [13] Sonny Homepage.
- [14] HONDA Homepage.

- [15] Segway Homepage.
- [16] California Energy Commission, 200kWe Solid Fuel Cell / Microturbine Generator Hybrid Proof of Concept Demonstration Report, March 2001.
- [17] Eito Matsuo, Haruo Yoshiki, Toshio Nagashima, and Chisahi Kato, Toward the development of the finger top gas turbines, IGTC '03 Tokyo.
- [18] Y. Ribaud, Internal Heat Mixing and External Heat Losses in an Ultra Micro Turbine, IGTC'03.
- [19] C. Kato, H. Yoshiki, E. Matsuo, H. Ikeda, and K. Nishimura, Prototyping of Small-sized Two-dimensional Radial Turbines, IGTC '03.
- [20] M.R. Galvas, Nasa TN D-6729, 1972.
- [21] S. Yuasa, K. Oshimi, and M. Uehara, Concept and Combustion Characteristics of a Ultra-micro and a Micro Combustor, IGTC-03.
- [22] M. Uehara, S. Yuasa, H. Yoshiki, E. Matsuo, Operating characteristics of propane combustors for kW class micro gas turbines, JSME, Mechanical engineering congress 2003 Japan, Aug. 2003 (Japanese).
- [23] Hayashi, K. and Hirasata, K., "Developments of Aerodynamic Foil Bearings for Small High-speed Rotor," Proc. of 21st Leeds-Lyon Symp., 291~299 (1994).
- [24] Kaneko, S., Watanabe, T., and Kitazawa, S., "Prototyping of Air Bearing for Micro Gas Turbine Use", Journal of JTSJ, Vol. 30, No. 4, pp. 283-287 (2002).
- [25] Kaneko, S., Kitazawa, S., and Watanabe, T., "Prototyping of Experimental Apparatus of Air Bearing for Microgasturbine", Proc.JSME, No. 02-76, Tokyo, 2002, pp. 553-556 (2002).
- [26] Kitazawa, S., Kaneko, S. and Watanabe, T., "Development of Foil Bearing for Micro Gas Turbine Use", IGTC2003, Tokyo, Japan, TS-019 (2003).
- [27] Kaneko, S., Watanabe, Y., Watanabe, T. and Kitazawa, S., "Prototyping of Radial and Thrust Foil Bearing for Small Size Micro Gas Turbines", Prep. JSME, No. 03-1(VI), Tokushima, 327-328 (2003).
- [28] Kaneko, S., and Mori, Y., "Natural Frequency Analysis of Palm Top Size Micro Gas Turbine Shaft System", Journal of JTSJ, Vol. 33, No. 1, pp. 25-31 (2005).
- [29] Kaneko, S., Miyano, Y., Mori, Y., and Watanabe, T., "Prototyping of palm top size micro gas turbine shaft system supported by foil bearings and the evaluation of dynamic characteristics", Journal of the Japan Institute of Energy, Vol. 84, No. 3, (2005), to appear.
- [30] Takao Nagasaki, Rinzo Tokue, Shoichi Kashima and Yutaka Ito, Conceptual Design of Recuperator for Ultra micro Gas Turbine, IGTC '03.
- [31] S. Hirado, T. Nagasaki, Y. Ito, Heat transfer analysis of UMG, JSME, No 8 Power and energy technology symposium, June 2002 (Japanese).
- [32] I.V. Gaydamaka, A.V. Efimov, M.Ja. Ivanov, O.I. Ivanov, R.Z. Nigmatullin, N.I. Ogarko, Some Aerodynamic Performances of Small Size Compressor and Turbine Stages, IGTC'03.
- [33] R.A. Van den Braembussche, A.A. İşlek, Z. Alsalihi, Aerothermal Optimization of Micro-gasturbine Compressor Including Heat Transfer.

